Chemical Engineering Journal 505 (2025) 159566

Contents lists available at ScienceDirect

Chemical Engineering Journal

journal homepage: www.elsevier.com/locate/cej

Large-Scale synthesis of crystalline phosphorus nanosheets with superior air-water stability and flame-retardancy ability

Zunbin Duan [a,b,1], Rui Li [a,c,1], He Bian [d], Yanfang Wang [a], Xue Zhang [a], Ziqiang Cheng [a,f], Danni Liu [a], Yang Li [a], Shuai Zhang [a], Guangbo Qu [e,h], Paul K. Chu [g], Jiahong Wang [a,h,*]

[a] Shenzhen Institute of Advanced Technology, Chinese Academy of Sciences, Shenzhen 518055 China
[b] National Engineering Research Center for Colloidal Materials and School of Chemistry and Chemical Engineering, Shandong University, Jinan 250100 China
[c] Beijing Key Laboratory for Green Catalysis and Separation, Department of Environmental Chemical Engineering, Beijing University of Technology, Beijing 100124 China
[d] Binzhou Key Laboratory of Material Chemistry, Department of Chemical Engineering and Safety, Shandong University of Aeronautics, Binzhou 256603 China
[e] State Key Laboratory of Environmental Chemistry and Ecotoxicology, Research Center for Eco-Environmental Sciences, Chinese Academy of Sciences, Beijing 100085 China
[f] Department of Applied Physics, East China Jiaotong University, Nanchang 330013 China
[g] Department of Physics, Department of Materials Science and Engineering, and Department of Biomedical Engineering, City University of Hong Kong, Tat Chee Avenue, Kowloon, Hong Kong, China
[h] University of Chinese Academy of Sciences, Beijing 100049 China

ARTICLE INFO

Keywords:
Crystalline phosphorus
Large-scale synthesis
Black phosphorus
Air–water stability
Flame retardancy

ABSTRACT

Black phosphorus (BP) has spurred exploration of two-dimensional phosphorus allotropes but its inferior stability in air and water as well as complex exfoliation routes hinder large-scale application. Herein, crystalline phosphorus nanosheets (cryst-P NSs) are synthesized by a solvothermal technique using amorphous red phosphorus and amine as the raw materials. The one-pot production weight of the cryst-P NSs with an average lateral size of 200 nm and thickness of 15 nm can be increased to 100 g with a high yield over 95%. The underlying mechanism of the amine promoted structure and transformation from amorphous to crystalline is systemically investigated, and an active amine screening model is proposed from the macroscopic perspective. The cryst-P NSs exhibit superior stability in different environments, including ambient conditions, humid air, aqueous solution, and light irradiation due to their weak surface hydrophilicity. Compared to emerging efficient flame retardant BP NSs, the cryst-P NSs possess better fire retarding properties. The amine-driven structural transformation paves the way for low-cost and large-scale production of nanomaterials, and the stable phosphorus allotrope is expected to have application in many and broader fields.

1. Introduction

Phosphorus is an abundant and essential element on earth and participates in many physicochemical processes spanning energy, agriculture, flame-retardancy, and medicine.[1,2] Among the common allotropes of phosphorus, black phosphorus (BP), a two-dimensional (2D) semiconductor with a puckered honeycomb layered structure, has drawn extensive interests for its high carrier mobility and tunable direct bandgap.[1,3] The interlayer van der Waals interactions facilitate the exfoliation of bulk BP into single or few-layer nanosheets (BP NSs) to fulfil the extraordinary potential.[3,4] Classical methods such as liquid phase exfoliation, ball milling, and electrochemical intercalation are proposed to prepare BP NSs with high production efficiency.[5] Recently, innovative techniques including laser thermal evaporation and chemical vapor deposition have been developed to complement aforementioned methods.[6–8] However, there is not a single approach that can simultaneously guarantee the quality, morphology, and performance of BP NSs. Meanwhile, commercial application of BP NSs is stifled by the poor stability in air and water.[9,10] Surface passivation layers can protect the BP NSs but usually adversely affect the physicochemical and electronic properties.[11,12] Therefore, as an option, direct synthesis of high-quality elementary phosphorus nanosheets with robust air and water resistance is highly desirable albeit challenging.

Wet-chemical bottom-up method has been explored for the synthesis

* Corresponding author.
E-mail address: jh.wang1@siat.ac.cn (J. Wang).
[1] Both authors contributed equally to this work.

https://doi.org/10.1016/j.cej.2025.159566
Received 7 September 2024; Received in revised form 11 December 2024; Accepted 12 January 2025
Available online 13 January 2025

of nano phosphorus.[13–16] The phosphorus atoms are directly dissolved and precipitated into nanoclusters or nanostructures, thereby skipping the high-temperature bulk crystal growth process and long-term exfoliation treatment.[17–20] White phosphorus and phosphorus halides have mainly been used as the raw reagents but they are toxic and flammable and the reaction is too dangerous to scale up for industrial production.[21,22] Thus, some organic amine assisted solvothermal methods have been developed and various elementary phosphorus nanodots or nanospheres have been synthesized. Nonetheless, the high amine residue, low crystallinity, and uncontrollable morphology impede the development of the wet-chemically synthesized elemental phosphorus based nanostructures.[15,23–26].

Herein, a simple wet-chemical technique is demonstrated to synthesize high-pure crystalline phosphorus nanosheets (cryst-P NSs) with uniform two-dimensional morphology, in which the as-prepared cryst-P NSs exhibit excellent stability in oxygen and water. By systemically exploring the effects of amine, massive cryst-P NSs with a lateral size of 200 nm and average thickness of 15 nm are synthesized from raw amorphous red phosphorus (amorph-P) microparticles. In comparison to BP NSs of comparable lateral size and thickness, the cryst-P NSs possess less surface hydrophilicity, leading to superior air and water resistance. Owing to the unique crystalline structure, the cryst-P NSs have obvious thermal stability and compared to the liquid-exfoliated BP NSs with a similar size and thickness, the cryst-P NSs exhibit superiority in flame retardancy. The cryst-P NSs with superb stability bode well for large-scale production, long-term storage, and excellent thermal stability rendering them promising in practical applications such as flame-retardancy, catalysis, and energy storage.

2. Experimental procedures

2.1. Materials

High-purity commercial amorphous red phosphorus (99.999%, 5 N) was purchased from Western Elements (Ningxia). Ethylenediamine ($C_2H_8N_2$; >99%; CAS 107–15-3), 1,3-propanediamine ($C_3H_{10}N_2$; 98%; CAS 109–76-2), 1,4-diaminobutane ($C_4H_{12}N_2$; 98%; CAS 110–60-1), 1,6-hexamethylenediamine ($C_6H_{16}N_2$; 99%; CAS 124–09-4), 1,8-diaminooctane ($C_8H_{20}N_2$; 98%; CAS 373–44-4), *N*-ethyl-1,2-ethanediamine ($C_4H_{12}N_2$; 98%; CAS 110–72-5), *N*,*N*-dimethylethylenediamine ($C_4H_{12}N_2$; 98%; CAS 108–00-9), *N*,*N*-diethylethylenediamine ($C_6H_{16}N_2$; 98%; CAS 100–36-7), *N*,*N*-diisopropylethylenediamine ($C_8H_{20}N_2$; 97%; CAS 121–05-1), *N*,*N*,*N*',*N*'-tetramethylethylenediamine ($C_6H_{16}N_2$; 99%; CAS 110–18-9), *N*-methyl-1,3-diaminopropane ($C_4H_{12}N_2$; 98%; CAS 6291–84-5), 3-dimethylamino-1-propylamine ($C_5H_{14}N_2$; 99%; CAS 109–55-7), 3-diethylamino-1-propylamine ($C_7H_{18}N_2$; 99%; CAS 104–78-9), *N*,*N*,2,2-tetramethyl-1,3-propanediamine ($C_7H_{18}N_2$; 98%; CAS 53369–71-4), diethylenetriamine ($C_4H_{13}N_3$; 99%; CAS 111–40-0), triethylenetetramine ($C_6H_{18}N_4$; 70%; CAS 112–24-3), tetraethylenepentamine ($C_8H_{23}N_5$; 95%; CAS 112–57-2), pentaethylenehexamine ($C_{10}H_{28}N_6$; CAS 4067–16-7), 1,2-bis(3-aminopropylamino)ethane ($C_8H_{22}N_4$; 97%; CAS 10563–26-5), *N*,*N*-bis(3-aminopropyl)methylamine ($C_7H_{19}N_3$; 98%; CAS 105–83-9), *N*,*N*-dimethyldipropylenetriamine ($C_8H_{21}N_3$; 99%; CAS 10563–29-8), and *n*-butylamine ($C_4H_{11}N$; 98%; CAS 109–73-9) were obtained from Aladdin Reagent. Black phosphorus nanosheets, type II red phosphorus, fibrous phosphorus (type IV red phosphorus), and violet phosphorus (type V red phosphorus) synthesized by chemical vapor transmission method were purchased from Mophos (*https://www.Mophos.cn*) and anhydrous ethanol (99.5%), *N*,*N*-dimethylformamide (DMF; 97%), *N*-methylpyrrolidone (NMP; 99.5%), dimethyl sulfoxide (DMSO; 99.5%), and acetone (99.5%) were obtained from Sinopharm Chemical Reagent. Deionized (DI) water purified by a Milli-Q Direct 8 purification system was used in the experiments. The epoxy resin CER1000 and curing agent CEH500 were obtained from Guangzhou Weiyee Metallographic Test Instrument Co. Ltd. All the reagents were used as received without further purification.

2.2. Synthesis of crystalline phosphorus by an amine-driven solvothermal technique

Crystalline phosphorus (cryst-P) was synthesized using a phosphorus source mixed with an amine with a certain source-to-solvent ratio at an elevated temperature. In the typical synthesis process of cryst-P nanosheets, the mixture was prepared with amorphous red phosphorus powder about 20 μm in size as the source and *N*-ethyl-1,2-ethanediamine as the solvent (1 g of phosphorus per 10 mL of solvent). The mixture was stirred for 30 min at room temperature (RT) to obtain a uniform suspension before introducing into a 25 mL polymerizedpolyethyleneliner (PPL) −lined stainless steel autoclave. The air in the autoclave was replaced with argon so that the reaction proceeded in an inert atmosphere. The autoclave was heated to 250 °C for 20 h and then cooled in air. The product was rinsed with DI water and anhydrous ethanol to remove unreacted species and solvents, and the orange solid sample was obtained by centrifugation at 13,000 rpm for 10 min. The centrifuge-wash cycle was repeated three times after which the solid was dried at 40 °C under vacuum to obtain the cryst-P NSs. 1,4-Diaminobutane, 1,6-hexamethylenediamine, and 1,8-diaminooctane are solid at RT. The source was 1 g of phosphorus per 10 g of solvent and mixing was performed at 70 °C to obtain a homogeneous suspension. In the large-scale synthesis of cryst-P NSs, 100 g of the red phosphorus powder and 200 mL of *N*-ethyl-1,2-ethanediamine were placed in a 400 mL PPL-lined stainless steel autoclave and the reaction time was 72 h. In the studied temperature range (120–280 °C), only one crystalline phosphorus allotrope is obtained, which is the cryst-P. The common solvents such as NMP, DMF, DMSO, ethanol, *etc.*, did not cause the crystal transformation of amorphous red phosphorus to produce the cryst-P.

Other procedures, including re-dispersion of cryst-P NSs, conductivity test, stability evaluation, preparation of P-based epoxy resin and bare epoxy resin, materials characterization, simulation and calculation, and calculation of flame-retardant parameters, are in the supplementary section.

3. Results and Discussion

3.1. Synthesis and characterization of crystalline phosphorus nanosheets

In the synthesis of cryst-P NSs, the raw amorphous red phosphorus powder is dispersed in amine (*e.g.*, *N*-ethyl-1,2-ethanediamine, $C_4H_{12}N_2$) and the uniform suspension is transferred to a PPL-lined stainless steel autoclave. The sealed autoclave is heated to 250 °C for 20 h to accomplish structural transformation. The solid product is centrifuged, washed, and vacuum-dried to obtain orange cryst-P NSs (Fig. 1a). This amine assisted wet-chemical synthesis procedure is easy to scale up. As shown in Fig. 1b, the weight of the product can be increased to 100 g and the conversion yield of the large-scale synthesis is maintained to be 95.6% (Fig. S1), indicating good industrial prospect. The purity of the cryst-P NSs is determined by combustion elemental analysis and energy-dispersive X-ray spectroscopy (Table S1 and Fig. S2), that the small nitrogen content suggests the rare amine remaining. The crystal structure of cryst-P NSs closely resembles that of the crystalline type II red phosphorus but differs from those of other allotropes synthesized by the conversional chemical vapor transmission (CVT) method, such as fibrous phosphorus (type IV red phosphorus), violet phosphorus (type V red phosphorus), and black phosphorus (Fig. S3).[27–36] The cryst-P NSs exhibit Raman scattering peaks at 352, 400, and 462 cm^{-1}, of which the strongest peak at 352 cm^{-1} corresponds to the stretching vibrations of P9 and P8 cages (Fig. S4).[34,37–39].

The cryst-P NSs are dispersed ultrasonically in ethanol to form a homogeneous orange suspension (inset in Fig. 1c). The well-defined 2D characteristics of cryst-P NSs is investigated by scanning electron microscopy (SEM), atomic force microscopy (AFM), transmission electron microscopy (TEM), and scanning transmission electron microscopy

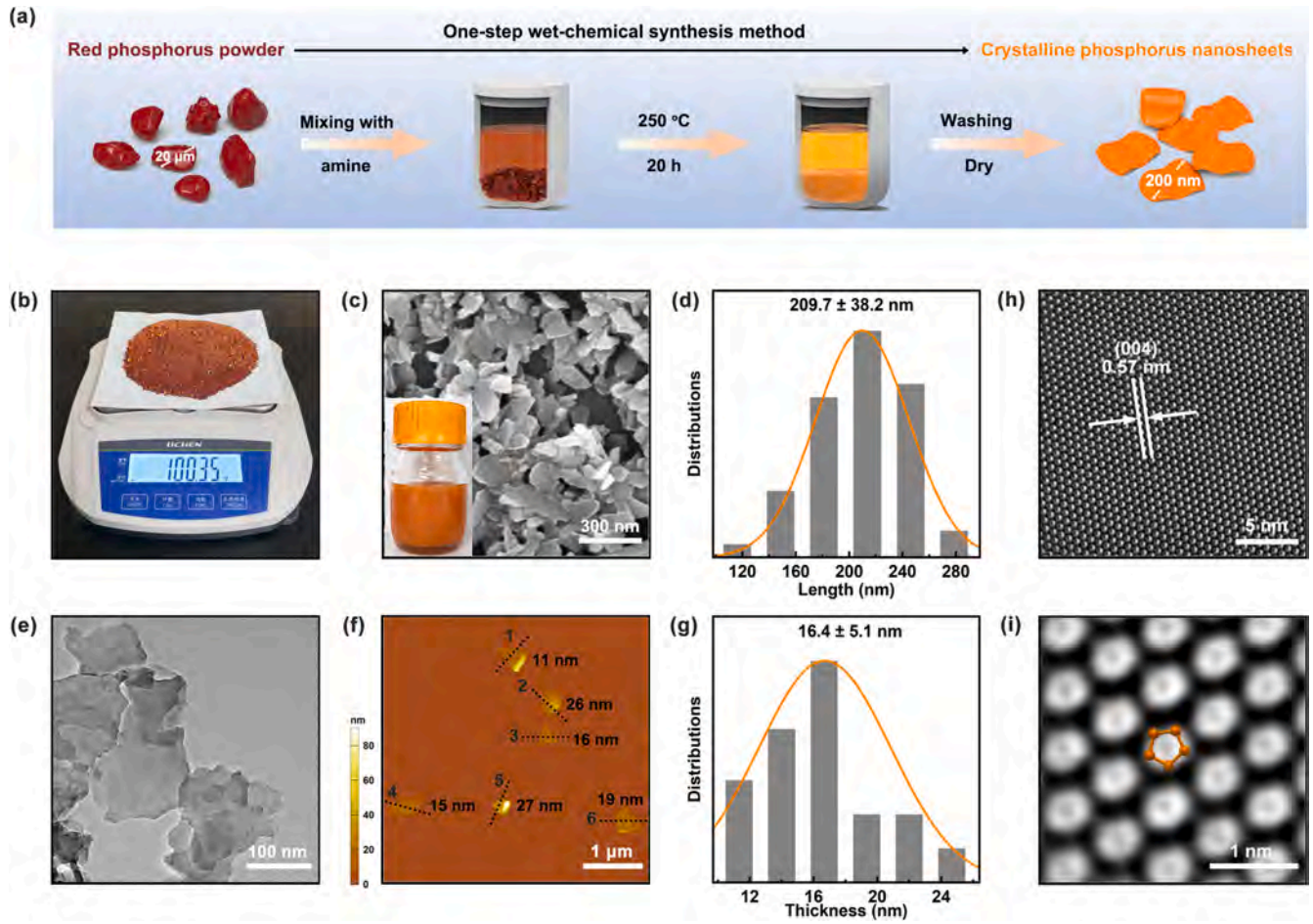

Fig. 1. Synthesis and characterization of the cryst-P NSs. (a) Schematic diagram of the synthesis of cryst-P NSs with a lateral size of about 200 nm using red phosphorus powder with a size of 20 μm. (b) White light photograph of the one-pot synthesized 100 g cryst-P NSs powder. (c) SEM image of the cryst-P NSs obtained from re-dispersed ultrasonication in ethanol (inset showing the photograph of the corresponding cryst-P NSs suspension). (d) Diameter distribution of the cryst-P NSs corresponds to the long axis. (e) TEM image of the cryst-P NSs. (f) AFM image of the cryst-P NSs with height profiles. (g) Thickness distribution of the cryst-P NSs. (h) Low magnification STEM image of the cryst-P NS. (i) High magnification HAADF-STEM image of the cryst-P NS showing the pentagon tubes. (For interpretation of the references to color in this figure legend, the reader is referred to the web version of this article.)

(STEM). The uniform lateral size of cryst-P NSs is 209.7 ± 38.2 nm, according to the SEM image and statistics (Figs. 1c and d). The fine 2D morphology of cryst-P NSs is further confirmed by TEM (Fig. 1e). The AFM profiles in Figs. 1f and g of the cryst-P NSs reveal a lateral size of 200 − 300 nm and thickness of 16.4 ± 5.1 nm, indicating exfoliation is not necessary to produce the nanosheets thereby simplifying the synthesis tremendously. The lattice fringe with a spacing of 0.57 nm (Fig. 1h) can be indexed to the (004) plane, and the cryst-P NS features the pentagon tubes shown in the atomic resolution high-angle annular dark-field STEM (HAADF-STEM) image of Fig. 1i, which aligns with the type II red phosphorus reported in 2023.[34].

3.2. *Amine-driven solvothermal mechanism for the production of cryst-P*

In the wet chemical synthesis of cryst-P NSs, the nucleophilic amines play a vital role. Phosphorus allotropes generally possess the electrophilic character and can be activated by nucleophiles like ethylenediamine.[21] However, previous reports demonstrate that highly crystalline phosphorus nanosheets are infrequently produced.[13,15,22,23,40] To elucidate the formation mechanism, diverse amines are screened to identify the optimal conditions as well as amine-promoted structure-reconstruction principle. As shown in Table 1a, diamines with different alkane chain lengths are used first. The diamine with a longer alkane chain is conducive to the formation of cryst-P, for example, 1,6-hexamethylenediamine ($C_6H_{16}N_2$) and 1,8-diaminooctane ($C_8H_{20}N_2$) (Fig. S5a). When diamines with shorter carbon chains are used, only the amine-enriched phosphorus (amine-P) can be obtained (Figs. S5a and S6; Table S1). The obvious difference may be associated with the different activation ability of different diamines.

The activation ability of amines is further modulated by using alkyl-substituted diamines with different steric hindrance to produce cryst-P NSs. As shown in Tables 1b and c, Figs. S5b and S5c, most mono-substituted or disubstituted 1,2-ethylenediamine and 1,3-propanediamine with methyl and ethyl groups can react with raw amorphous red phosphorus to produce cryst-P NSs. Besides, the substituted diamine like *N*,*N*-diisopropylethylenediamine ($C_8H_{20}N_2$) shows great steric hindrance and only unreacted amorphous phosphorus (amorph-P) is observed from the final product (Table S1 and Fig. S5b). In addition to alkyl-substituted diamines, amines containing multiple amino groups are used to investigate the amine selection rule for the synthesis of cryst-P NSs (Table 1d). Along with the decrease in the total ratio of primary amino groups to secondary amino groups, the cryst-P NSs are generated, and tetraethylenepentamine ($C_8H_{23}N_5$) and pentaethylenehexamine ($C_{10}H_{28}N_6$) are suitable for the synthesis of cryst-P NSs (Fig. S5d).

To evaluate the impact of amines on the synthesis of cryst-P NSs, the conductivities of the different amine suspensions of raw amorph-P are determined at 70 °C (Fig. 2a-1 and Table S2). A higher conductivity shows that more ionized species are produced, indicating the stronger

Table 1
Synthesis of the cryst-P using different linear amines. (a) Diamine with different chain lengths, (b) Substituted 1,2-ethylenediamine, (c) Substituted 1,3-propanediamine, and (d) Amine with multiple amino groups.

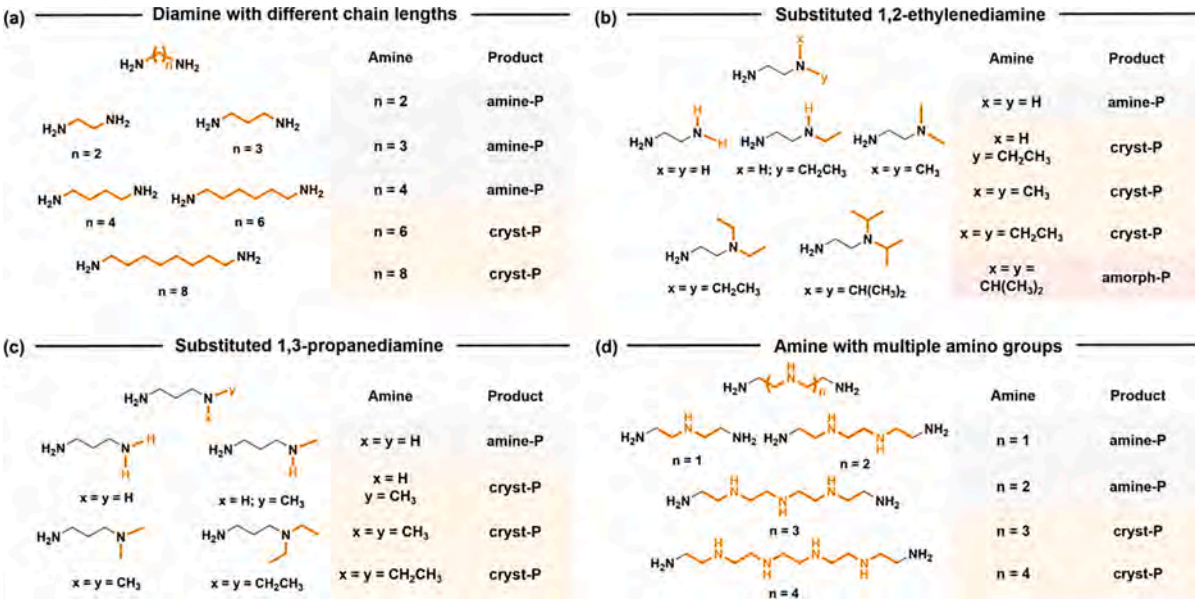

activation ability of the amine. For instance, the conductivities of the raw amorph-P dissolved suspensions in 1,6-hexamethylenediamine (3.41 μS cm^{-1}) and 1,8-diaminooctane (0.22 μS cm^{-1}) are much smaller than those in 1,2-ethylenediamine ($C_2H_8N_2$), 1,3-propanediamine ($C_3H_{10}N_2$), and 1,4-diaminobutane ($C_4H_{12}N_2$) (the values of all these suspensions are larger than 80 μS cm^{-1}). Our findings suggest that the formation of cryst-P NSs is correlated with the activation ability of the amines and excessive amine-phosphorus activation leads to the generation of amine-P. In comparison, amines with too many alkane groups show nearly zero conductivity and extremely weak ability to dissolve phosphorus. As a result, in the case of the amines such as *N*-ethyl-1,2-ethanediamine, 3-dimethylamino-1-propylamine ($C_5H_{14}N_2$), and tetraethylenepentamine, rarely reacted amorphous phosphorus exists in the products and the conductivities of the dispersions are in the range of 0.087–26.6 μS cm^{-1} as summarized in Fig. 2a-1 and Table S2.

The amine equivalent is a classical descriptor of the amine activity, which can be calculated by dividing the molecular weight of the amine by the number of active hydrogens. Herein, the values of amine equivalent of different amines are calculated to predict the suitable linear amine for possible cryst-P production. As shown in Fig. 2a-2 and Table S2, the suitable amine equivalent value for producing cryst-P ranges from 27.04 to 65.12. We further use this standard to search for the best amines. As shown in Figs. 2b and S5e, four kinds of amines are applied to the synthesis of cryst-P, including 1,2-bis(3-aminopropylamino)ethane ($C_8H_{22}N_4$), *N*,*N*-bis(3-aminopropyl)methylamine ($C_7H_{19}N_3$), *N*,*N*-dimethyldipropylenetriamine ($C_8H_{21}N_3$), and *n*-butylamine ($C_4H_{11}N$). The conductivities of these amines containing raw phosphorus are measured and these four linear amines show conductivities between 0.97 μS cm^{-1} and 20.6 μS cm^{-1}. In general, the amine equivalent can serve as a reliable guidance to choose the appropriate solvent in the amine-driven cryst-P synthesis.

To achieve a more profound comprehension of the formation of cryst-P, the reaction between different amino groups and phosphorus is explored by simulating N–P bonds. *N*-Ethyl-1,2-ethanediamine [$NH_2(CH_2)_2NHCH_2CH_3$] containing one primary amino group and one secondary amino group is selected as the representative amine molecule. In the simulation, the pyramidal P_4 cluster (a subunit structure in amorphous red phosphorus) is activated by the secondary amino group (*path 1*) and primary amino group (*path 2*), respectively. Regardless of whether the P_4 cluster is activated by the secondary or primary amino group, the closed pyramidal structure is transformed into the open rhombic structure because of the strong N–P interaction (Fig. S7). The N–P bonding energy of the secondary amine linked with the P_4 cluster (292.77 kJ mol^{-1}) is smaller than that of primary amine (347.41 kJ mol^{-1}), suggesting that the N–P bond formed on the secondary amine is easier to break to release the open rhombic P_4 clusters (Fig. S7 and Table S3). Consequently, the rhombic P_4 cluster can be polymerized into larger phosphorus molecules thermodynamically, which is resulting in crystallization to form cryst-P.[39] Because the amine-driven cryst-P NSs growth method proceeds at a much lower temperature than that in the CVT process (ca. 250 °C *vs.* 500 °C), lower energy consumption entails and meanwhile, the uniform 2D morphology renders complex and prolong exfoliation unnecessary.[4,40–42].

3.3. Air and water stability of cryst-P NSs in different environments

Water and oxygen easily cause decomposition of BP nanosheets, hence the stability in air and water is very important to applications of phosphorene.[9,10,43,44] The water contact angles on the cryst-P NSs and BP NSs with a similar size and thickness (Figs. 1 and S8) are measured to study the surface hydrophilicity, as shown in Figs. 3a and S9. The initial water contact angle on the cryst-P NSs is 45.2° ± 0.4° and about three times that on the BP NSs (15.6° ± 0.6°). The contact angles on the cryst-P NSs decrease slowly and that of 33.1° ± 0.6° after 240 s remains much larger than the initial contact angle on the BP NSs, implying that the cryst-P NSs are less hydrophilic than the BP NSs and may show superior stability and dispersion in matrix.

The stability in air and water of the cryst-P NSs is further verified experimentally under four different conditions of ambient-air, water-saturated air, heating-water, and radiant-water. The morphological change in the single cryst-P NS is monitored by AFM under ambient conditions (25 °C, 37% humidity; Figs. 3b and S10). The cryst-P NS exhibits a smooth surface without droplets after continuously aging for 72 h, which is different from the BP NS in air. This reveals the resistance of cryst-P NSs against oxidation. The stability in water-saturated air is then evaluated. The cryst-P NSs and BP NSs with a similar lateral size

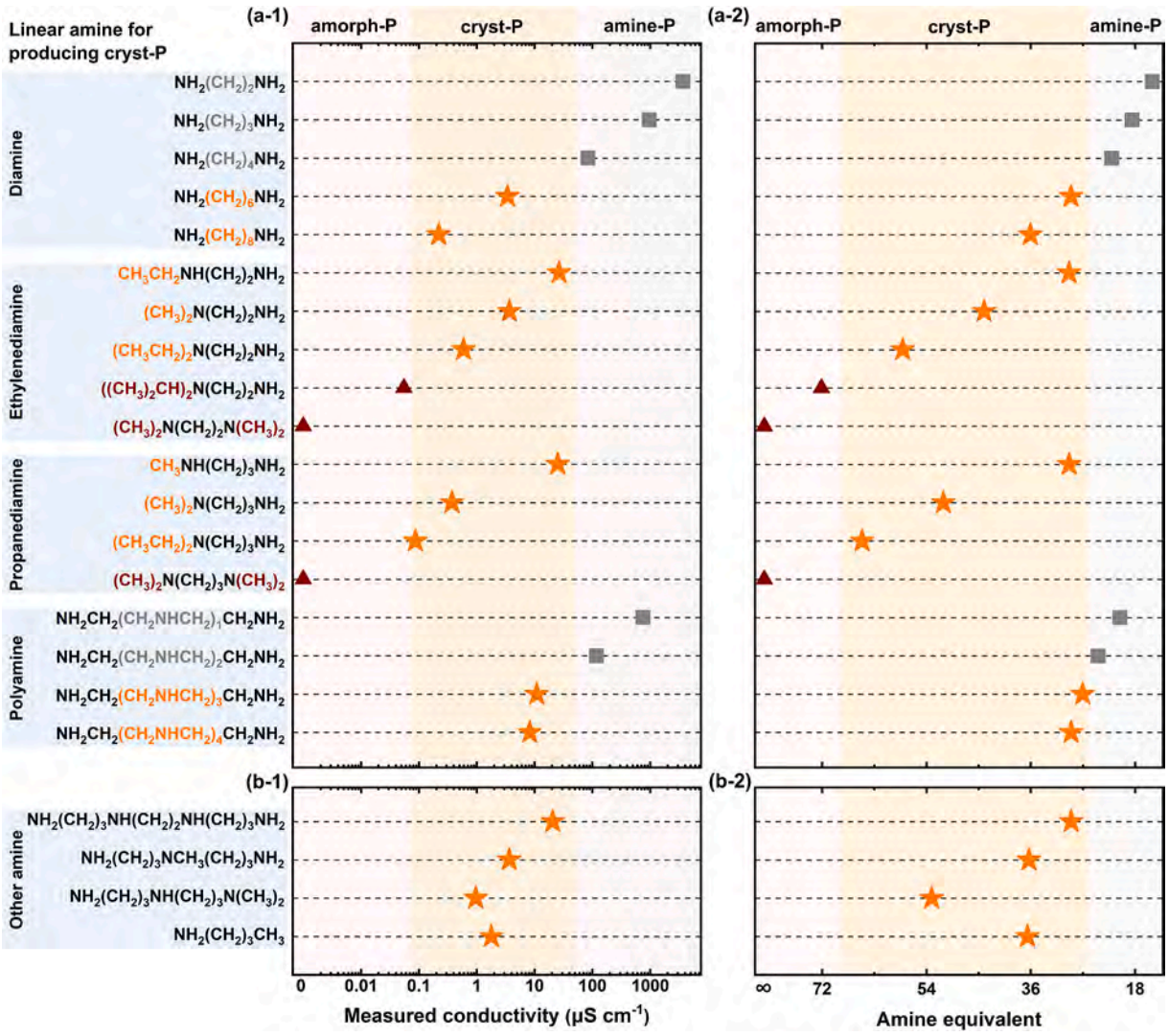

Fig. 2. Linear amines for the production of the cryst-P. (a) Summarized results of different amines and corresponding physicochemical parameters: (a-1) Measured conductivities of the red phosphorus suspension for different amines and (a-2) Calculated amine equivalent values. (b) Four linear amines used in the production of cryst-P, which are predicted by the amine equivalent rule: (b-1) Measured conductivities of the red phosphorus suspensions with the four different amines and (b-2) Calculated amine equivalent values of the four amines. (For interpretation of the references to color in this figure legend, the reader is referred to the web version of this article.)

and thickness are exposed to water-saturated air (≥99% humidity) for 120 h and detected by X-ray photoelectron spectroscopy (XPS). As presented in Figs. 3c and S11a,b, elemental phosphorus is indicated by the *P* $2p_{3/2}$ peak at 129.5 eV and *P* $2p_{1/2}$ peak at 130.5 eV and the peak at 134.0 eV arises from oxidized phosphorus (P_xO_y). The P_xO_y content in the cryst-P NSs increases only slightly after 24 h and a considerable amount of elemental phosphorus remains after 120 h. The ratios of the integrated area under the *P* $2p_{1/2}$ and *P* $2p_{3/2}$ peaks [*Area (P)*] to that under the P_xO_y peak [*Area* (P_xO_y)] are calculated to evaluate the extent of oxidization (Table S4, Figs. 3d and S11c). The area ratios of cryst-P NSs decrease more slowly than those of BP NSs, indicating that elemental P in cryst-P NSs is only partially converted to oxide.

In actual applications, phosphorus nanosheets are often submerged in water and so the stability in the aqueous environment is of utmost importance.[1,45] The water suspension containing the cryst-P NSs or BP NSs after different storage druations is photographed and studied by absorption spectroscopy. Since the temperature is critical to decomposition of nanomaterials, the test temperature is 30, 40, and 50 °C (Figs. 3e, f and S12). The color of the cryst-P NSs suspension remains orange after storage for 120 h at all three temperatures but the aqueous suspension with BP NSs is almost transparent. Moreover, if the aqueous solution containing cryst-P NSs is irradiated by a xenon lamp for 10 h, the suspension color is nearly constant and the absorption intensity is maintained at 93% of the initial value (Fig. S13). The long-term storage stability is evaluated. After being aged for over one year (approximately 13 months), the ethanol suspension of the cryst-P NSs maintains the orange color and pristine crystal structure with extremely low degree of oxidation (see Fig. S14). Compared to type II red phosphorus nanorods synthesized by CVT method, the cryst-P NSs exhibit good stability in water at 60 °C (Fig. S15). These results confirm the superior stability of the cryst-P NSs.

3.4. Fire retardancy properties of cryst-P NSs

Flame retardancy is another important issue in applications, and flame-retardant additives can effectively react with chemical species in the flame to terminate combustion.[46–49] Developing halogen-free flame retardants is a significant trend to address toxicity and bioaccumulation concerns and inorganic phosphorus-based flame retardants with high-efficiency, low-toxicity, and non-polluting characteristics are emerging alternatives.[50–52] The red phosphorus flame retardant currently used is micron-sized and requires a large

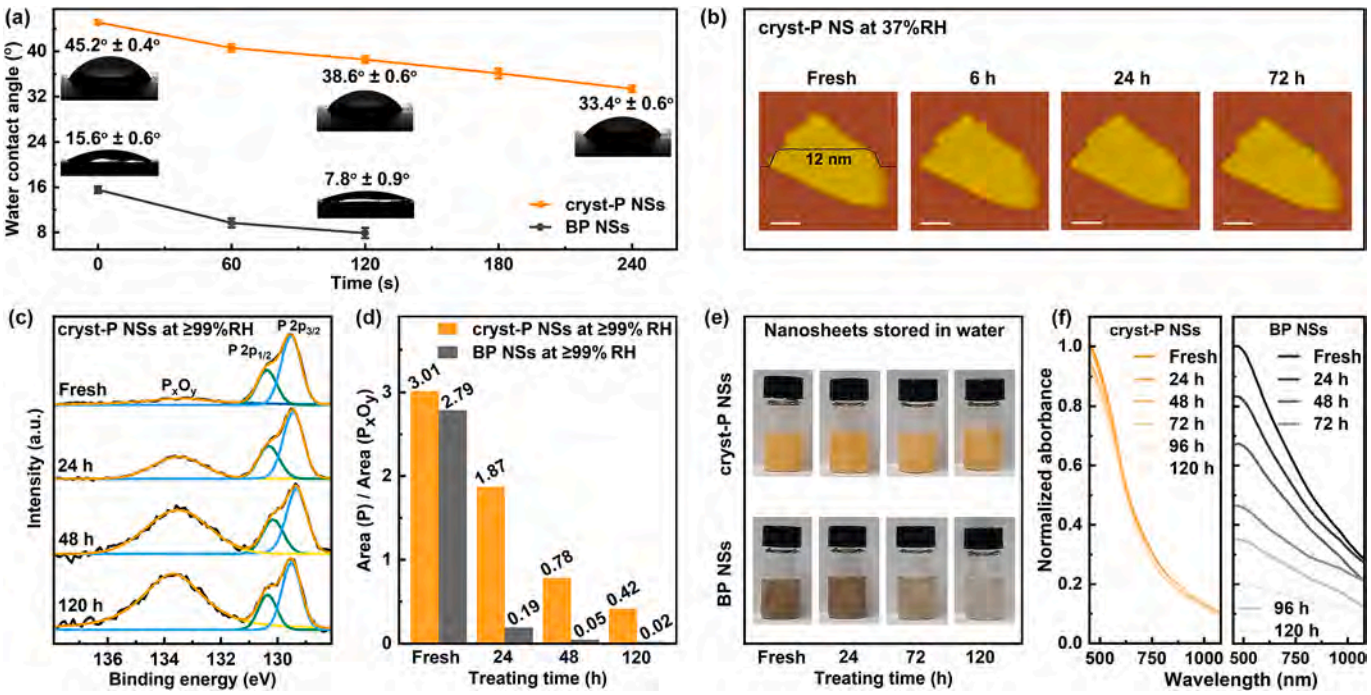

Fig. 3. Air and water stability of the cryst-P NSs. (a) Water contact angles on the cryst-P NSs and BP NSs. (b) Stability in ambient-air of one cryst-P NS (25 °C, 37% humidity), AFM graphs of the cryst-P NS with a thickness of 12 nm (scale bars, 100 nm). (c, d) Stability in water-saturated air for the cryst-P NSs (35 °C, ≥99% humidity): (c) XPS spectra of the cryst-P NSs; (d) Integrated area ratios of elemental phosphorus [*Area(P)*] to P_xO_y [*Area(P_xO_y)*]. (e, f) Stability in water of the cryst-P NSs at 30 °C: (e) Photographs of the water suspensions of cryst-P NSs and BP NSs; (f) Absorption spectra of cryst-P NSs and BP NSs. The BP NSs are produced by ultrasonic liquid-exfoliation of BP crystals and close to the cryst-P NSs with respect to the size and thickness (Fig. S8).

amount of addition (usually > 5.0 wt%) to meet the application requirements.[53] Particle morphology exerts a pivotal influence on flame retardancy, of which the 2D layered structure exhibits superb flame-retardant properties compared to the tubular and spherical structures.[54,55] BP nanosheets demonstrate favorable flame retardancy owing to their phosphorus-rich construction and layered structure; however, they are challenging to align with the requirements of rigorous industrial scenarios due to their inferior stability and complex exfoliation.[56] The salable synthesis, air–water stability, two-dimensional morphology, and uniform nano size of cryst-P NSs bode well for flame-retardancy.

The flame retarding properties of cryst-P NSs are investigated in the important thermosetting plastic of epoxy resin (EP).[57,58] The cryst-P NSs and the BP NSs with similar size/thickness are dispersed in EP to form the cryst-P NSs/EP and BP NSs/EP composites with an addition amount of 1.0 wt%, respectively. To determine the fire retardancy properties, the open flame test in the laboratory (*ca.* 25 °C, 37% humidity; differs from the UL-94 test) is conducted first. As shown in Fig. 4a, when the cryst-P NSs/EP is exposed to fire, the surface is ignited and then burns slowly. In contrast, the BP NSs/EP and bare EP burn rapidly. The thermal stability is an essential parameter of flame-retardant additives because in direct wet-chemical synthesis, there are less post-treatment induced defects in the cryst-P NSs than the liquid exfoliated BP NSs. In the thermogravimetric analysis (TGA) results under nitrogen shown in Fig. 4b, the temperature of the maximum weight loss rate of cryst-P NSs (435 °C) is higher than that of BP NSs (397 °C) indicative of good thermal stability of the cryst-P NSs, further confirmed by the thermogravimetric results under dried air and undried air containing trace amounts of water in Fig. S16. Therefore, the cryst-P NSs owning good dispersion effects in matrix (validated by optical micrographs and SEM-mappings in the cross-sections of composites illustrated in Fig. S17) can act as an effective barrier to prevent diffusion of volatile substances. After the thermal decomposition of the phosphorus added EP composites, the residual weight of the cryst-P NSs/EP is 10.28% that is higher than those of the BP NSs/EP (5.60%) and bare EP (4.70%) (Figs. 4c and S18). The high carbon residue demonstrates that the cryst-P NSs have excellent carbonization catalytic ability.

The test environment in cone calorimetry is close to the real combustion environment and cone calorimetry is widely used to evaluate the combustion properties of materials.[59] The heat release, smoke generation, and toxic carbon monoxide (CO) production are investigated in the cone calorimetry test performed on the cryst-P NSs/EP, BP NSs/EP and bare EP. As shown in Fig. 4d, the bare EP burns quickly and produces large peak of heat release rate (pHRR) and total heat release (THR). Both the cryst-P NSs/EP and the BP NSs/EP have smaller pHRR and THR. The cryst-P NSs have more impact on the heat release, and the pHRR and THR are reduced by 24.73% and 21.56% for the cryst-P NSs/EP, respectively. Fig. 4e shows the smoke production rate (SPR) and total smoke production (TSP) of the three samples. Smoke generation is mainly related to burning of polycyclic molecules in EP.[57] Of the three samples, the cryst-P NSs/EP shows the smallest SPR and TSP. Owning to the delayed release and capture of volatile species by the cryst-P NSs, the peak of SPR (pSPR) and TSP decrease by 59.68% and 35.56%, respectively. Suppression of CO release during combustion is essential to controlling the toxicity. As shown in Fig. 4f, the CO production rate (COPR) and total CO production (TCOP) from the cryst-P NSs/EP is less than those from the BP NSs/EP and bare EP. For the cryst-P NSs/EP, the peak of COPR (pCOPR) and TCOP are reduced by 47.09% and 35.61%, respectively. The reduction ratios of all combustion parameters are summarized in Fig. 4g. Compared to liquid-exfoliated BP NSs of similar size and thickness, the wet-chemically synthesized cryst-P NSs exhibit superior flame retardancy ability for delaying the combustion of EP, based on the results of cone calorimetry, microcalorimetry, limit oxygen index, and UL-94 (Figs. 4 and S19, Table S5).

According to aforementioned investigations and supporting references [48–50,53,54,60,61], the flame-retardant mechanism of cryst-P NSs is proposed (Fig. 4h). The cryst-P NSs with two-dimensional morphology are well dispersed in the substrate EP to act as a physical

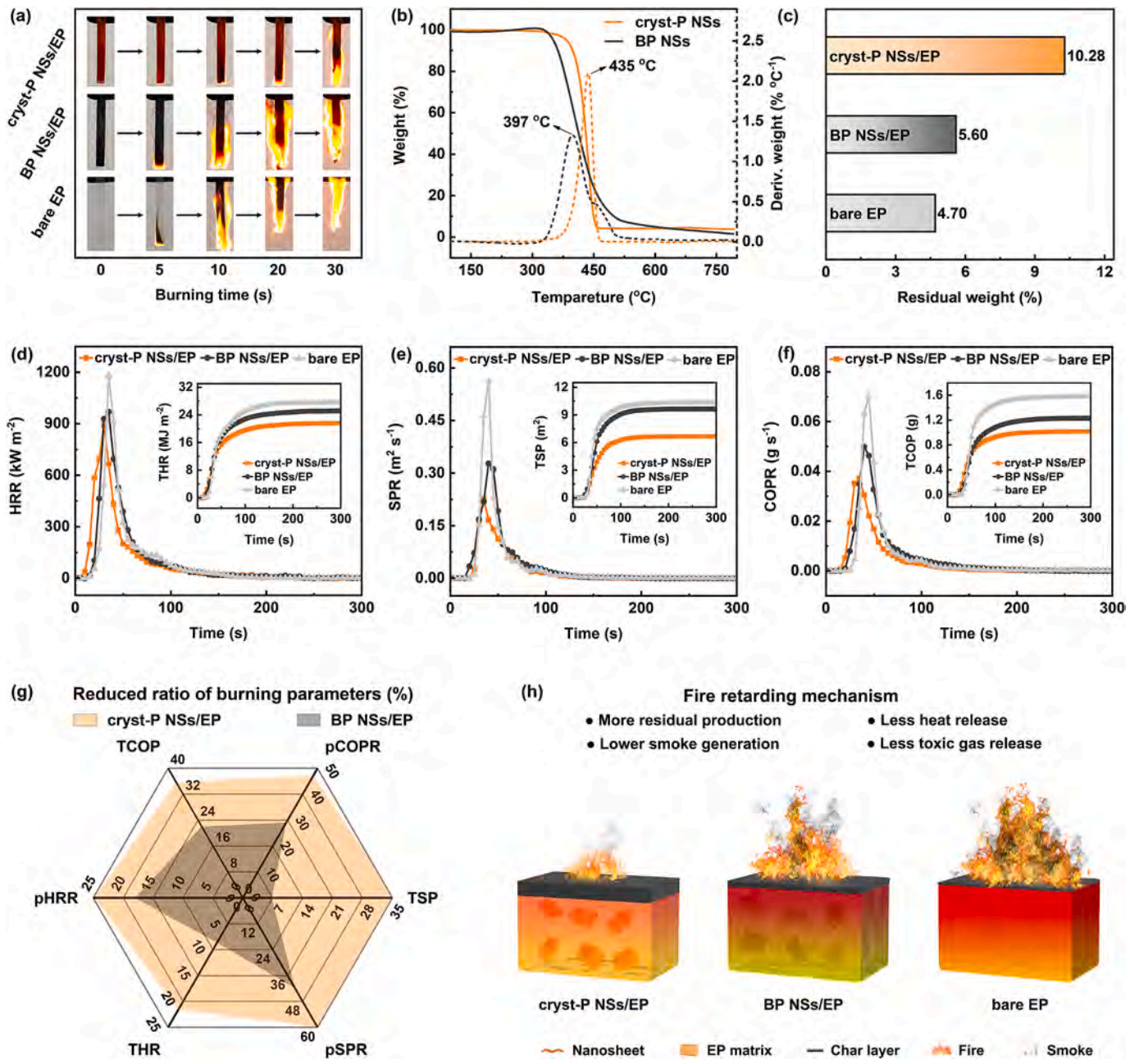

Fig. 4. Fire retardancy properties of the cryst-P NSs. (a) Photographs of the combustion processes of cryst-P NSs/EP, BP NSs/EP, and bare EP. (b) TG and differential TG curves of pure wet-chemically synthesized cryst-P NSs and liquid-exfoliated BP NSs under nitrogen. (c) Residual weights of cryst-P NSs/EP, BP NSs/EP, and bare EP. (d-f) Main parameters of the three samples tested by cone calorimetry: (d) HRR with inset of THR, (e) SPR with inset of TSP, and (f) COPR with inset of TCOP. (g) Improved degree of burning parameters of cryst-P NSs/EP and BP NSs/EP (reduced ratio of burning parameters calculated by equations S1–S6). (f) Fire retarding mechanism of cryst-P NSs/EP according to the formation of a physical barrier, catalytic carbonization, and the capture of pyrolysis free radicals. The BP NSs are produced by ultrasonic liquid-exfoliating BP bulk crystals and have similar size and thickness as the cryst-P NSs.

barrier leading to good thermal stability. Before decomposition, the barrier effect of cryst-P NSs delays the volatilization of the components and heat release. During decomposition, the cryst-P NSs catalyze carbonization of the residues and capture pyrolysis free radicals to inhibit heat transfer and improve the fire resistance. The as-synthesized cryst-P NSs show notable improvements of flame retardancy and mechanical properties in comparison to the BP NSs (Fig. S20), previously reported 2D inorganic flame retardants (Table S6), and commercial micron-sized amorph-P additive (Fig. S21a) and moreover, the low-cost and safe synthesis of cryst-P NSs (Fig. S21b) is a big advantage for next-generation efficient halogen-free flame retardants. In addition, as a *p*-type semiconductor (Fig. S22), the cryst-P NSs may have broad prospects in optoelectronic and catalytic applications.

4. Conclusion

Crystalline phosphorus nanosheets are synthesized by a scalable amine-driven solvothermal method. This process not only obviates the long-term and complex exfoliation treatment, but also realizes one-pot synthesis of 100 g of products with a high yield exceeding 95%. The cryst-P NSs possess a uniform 2D morphology with a size of about 200 nm and thickness of 15 nm. Amines play a crucial role in generating cryst-P NSs and the amine equivalent value is utilized to evaluate the amine-driven transformation from amorphous phosphorus to cryst-P

NSs, and the suitable conductivity of the red phosphorus amine-suspension is 0.087–26.6 μS cm^{-1}. Owing to the weak surface hydrophilic properties, the cryst-P NSs exhibit remarkable stability under various conditions, including atmosphere, highly humid air, aqueous, and organic solutions and are obviously better than the liquid-exfoliated BP NSs with a similar size and thickness. Moreover, the good thermal stability endows the cryst-P NSs with superior flame retardancy. The findings provide insights into the facile synthesis of 2D materials and unique properties of stable phosphorus allotropes.

CRediT authorship contribution statement

Zunbin Duan: Writing – original draft, Methodology, Investigation, Funding acquisition, Data curation, Conceptualization. **Rui Li:** Writing – original draft, Methodology, Investigation, Funding acquisition, Data curation. **He Bian:** Visualization, Investigation. **Yanfang Wang:** Data curation. **Xue Zhang:** Methodology, Investigation, Funding acquisition. **Ziqiang Cheng:** Investigation, Funding acquisition. **Danni Liu:** Data curation. **Yang Li:** Investigation. **Shuai Zhang:** Investigation. **Guangbo Qu:** Methodology, Investigation, Conceptualization. **Paul K. Chu:** Writing – review & editing, Funding acquisition. **Jiahong Wang:** Writing – review & editing, Supervision, Project administration, Funding acquisition, Conceptualization.

Declaration of competing interest

The authors declare that they have no known competing financial interests or personal relationships that could have appeared to influence the work reported in this paper.

Acknowledgements

Financial supports were provided by the National Natural Science Foundation of China (Nos. 22378007 and 62365010), the Youth Innovation Promotion Association Chinese Academy of Sciences (No. 2020354), the Guangdong Basic and Applied Basic Research Foundation (Nos. 2023A1515012957 and 2024A1515030176), the Shenzhen Science and Technology Program (No. JCYJ20220818100806014), the Shandong Provincial Natural Science Foundation (No. ZR2024QB029), the Shandong University of Aeronautics Research Funds (No. 2023Y19), the Jiangxi Provincial Cultivation Program for Academic and Technical Leaders of Major Disciplines (No. 20232BCJ23011), and the City University of Hong Kong Strategic Research Grant (SRG No.7005505).

Appendix A. Supplementary data

Supplementary data to this article can be found online at https://doi.org/10.1016/j.cej.2025.159566.

Data availability

Data will be made available on request.

References

[1] H. Tian, J. Wang, G. Lai, Y. Dou, J. Gao, Z. Duan, X. Feng, Q. Wu, X. He, L. Yao, L. Zeng, Y. Liu, X. Yang, J. Zhao, S. Zhuang, J. Shi, G. Qu, X.F. Yu, P.K. Chu, G. Jiang, Renaissance of elemental phosphorus materials: properties, synthesis, and applications in sustainable energy and environment, Chem. Soc. Rev. 52 (2023) 5388–5484, https://doi.org/10.1039/d2cs01018f.

[2] K. Wang, G. Yuan, Z. Liu, H. Yang, Y. Li, X. Li, K. Wu, J. Shi, Peacock flaunting tail inspired-multiple interactions between black phosphorene and glass powder with safety shield fire of epoxy resin, Chem. Eng. J. 485 (2024) 149846, https://doi.org/10.1016/j.cej.2024.149846.

[3] L. Li, Y. Yu, G.J. Ye, Q. Ge, X. Ou, H. Wu, D. Feng, X.H. Chen, Y. Zhang, Black phosphorus field-effect transistors, Nat. Nanotechnol. 9 (2014) 372–377.

[4] L. Zeng, X. Zhang, Y. Liu, X. Yang, J. Wang, Q. Liu, Q. Luo, C. Jing, X. Yu, G. Qu, P. K. Chu, G. Jiang, Surface and interface control of black phosphorus, Chem 8 (2022) 632–662, https://doi.org/10.1016/j.chempr.2021.11.022.

[5] G. Qu, T. Xia, W. Zhou, X. Zhang, H. Zhang, L. Hu, J. Shi, X. Yu, G. Jiang, Property-activity relationship of black phosphorus at the nano-bio interface: from molecules to organisms, Chem. Rev. 120 (2020) 2288–2346, https://doi.org/10.1021/acs.chemrev.9b00445.

[6] C. Chen, Y. Yin, R. Zhang, Q. Yuan, Y. Xu, Y. Zhang, J. Chen, Y. Zhang, C. Li, J. Wang, J. Li, L. Fei, Q. Yu, Z. Zhou, H. Zhang, R. Cheng, Z. Dong, X. Xu, A. Pan, K. Zhang, J. He, Growth of single-crystal black phosphorus and its alloy films through sustained feedstock release, Nat. Mater. 22 (2023) 717–724, https://doi.org/10.1038/s41563-023-01516-1.

[7] Y. Xu, X. Shi, Y. Zhang, H. Zhang, Q. Zhang, Z. Huang, X. Xu, J. Guo, H. Zhang, L. Sun, Z. Zeng, A. Pan, K. Zhang, Epitaxial nucleation and lateral growth of high-crystalline black phosphorus films on silicon, Nat. Commun. 11 (2020), https://doi.org/10.1038/s41467-020-14902-z.

[8] Z. Wu, Y. Lyu, Y. Zhang, R. Ding, B. Zheng, Z. Yang, S.P. Lau, X.H. Chen, J. Hao, Large-scale growth of few-layer two-dimensional black phosphorus, Nat. Mater. 20 (2021) 1203–1209, https://doi.org/10.1038/s41563-021-01001-7.

[9] T. Zhang, Y. Wan, H. Xie, Y. Mu, P. Du, D. Wang, X. Wu, H. Ji, L. Wan, Degradation chemistry and stabilization of exfoliated few-layer black phosphorus in water, J. Am. Chem. Soc. 140 (2018) 7561–7567, https://doi.org/10.1021/jacs.8b02156.

[10] Q. Zhou, Q. Chen, Y. Tong, J. Wang, Light-induced ambient degradation of few-layer black phosphorus: mechanism and protection, Angew. Chem., Int. Ed. 55 (2016) 11437–11441, https://doi.org/10.1002/anie.201605168.

[11] Y. Abate, D. Akinwande, S. Gamage, H. Wang, M. Snure, N. Poudel, S.B. Cronin, Recent progress on stability and passivation of black phosphorus, Adv. Mater. 30 (2018) 1704749, https://doi.org/10.1002/adma.201704749.

[12] K.L. Walz Mitra, C.H. Chang, M.P. Hanrahan, J. Yang, D. Tofan, W.M. Holden, N. Govind, G.T. Seidler, A.J. Rossini, A. Velian, Surface functionalization of black phosphorus with nitrenes: identification of P=N bonds by using isotopic labeling, Angew. Chem., Int. Ed. 60 (2021) 9127–9134, https://doi.org/10.1002/anie.202016033.

[13] Y. Zhang, X. Rui, Y. Tang, Y. Liu, J. Wei, S. Chen, W.R. Leow, W. Li, Y. Liu, J. Deng, B. Ma, Q. Yan, X. Chen, Wet-chemical processing of phosphorus composite nanosheets for high-rate and high-capacity lithium-ion batteries, Adv. Energy Mater. 6 (2016) 1502409, https://doi.org/10.1002/aenm.201502409.

[14] Y. Xu, Z. Wang, Z. Guo, H. Huang, Q. Xiao, H. Zhang, X. Yu, Solvothermal synthesis and ultrafast photonics of black phosphorus quantum dots, Adv. Opt. Mater. 4 (2016) 1223–1229, https://doi.org/10.1002/adom.201600214.

[15] Y. Li, S. Jiang, Y. Qian, Y. Han, J. Zhou, T. Li, L. Xi, N. Lin, Y. Qian, Amine-induced phase transition from white phosphorus to red/black phosphorus for Li/K-ion storage, Chem. Commun. 55 (2019) 6751–6754, https://doi.org/10.1039/c9cc02971k.

[16] J. Batur, Z. Duan, R. Jin, R. Li, Y. Xie, X. Yu, J. Li, Enhanced catalytic activity of crystalline phosphorus nanosheets fabricated *via* solvothermal phase transformation, Inorg. Chem. 63 (2024) 11860–11869, https://doi.org/10.1021/acs.inorgchem.4c01757.

[17] J. Mo, Y. Xu, L. Zhu, W. Wei, J. Zhao, A cysteine-mediated synthesis of red phosphorus nanosheets, Angew. Chem., Int. Ed. 60 (2021) 12524–12531, https://doi.org/10.1002/anie.202101486.

[18] A. Dragulescu-Andrasi, L.Z. Miller, B. Chen, D.T. McQuade, M. Shatruk, Facile conversion of red phosphorus into soluble polyphosphide anions by reaction with potassium ethoxide, Angew. Chem., Int. Ed. 128 (2016) 3972–3976, https://doi.org/10.1002/ange.201511186.

[19] M. Scheer, G. Balázs, A. Seitz, P_4 activation by main group elements and compounds, Chem. Rev. 110 (2010) 4236–4256, https://doi.org/10.1021/cr100010e.

[20] M. Jo, A. Dragulescu-Andrasi, L.Z. Miller, C. Pak, M. Shatruk, Nucleophilic activation of red phosphorus for controlled synthesis of polyphosphides, Inorg. Chem. 59 (2020) 5483–5489, https://doi.org/10.1021/acs.inorgchem.0c00108.

[21] B. Tian, B. Tian, B. Smith, M.C. Scott, Q. Lei, R. Hua, Y. Tian, Y. Liu, Facile bottom-up synthesis of partially oxidized black phosphorus nanosheets as metal-free photocatalyst for hydrogen evolution, P. Natl. Acad. Sci. USA 115 (2018) 4345–4350, https://doi.org/10.1073/pnas.1800069115.

[22] W. Chang, K. Tseng, H. Tuan, Solution synthesis of iodine-doped red phosphorus nanoparticles for lithium-ion battery anodes, Nano Lett. 17 (2017) 1240–1247, https://doi.org/10.1021/acs.nanolett.6b05081.

[23] W. Liu, S. Ju, X. Yu, Phosphorus-amine-based synthesis of nanoscale red phosphorus for application to sodium-ion batteries, ACS Nano 14 (2020) 974–984, https://doi.org/10.1021/acsnano.9b08282.

[24] B.M. Barry, E.G. Gillan, Low-temperature solvothermal synthesis of phosphorus-rich transition-metal phosphides, Chem. Mat. 20 (2008) 2618–2620, https://doi.org/10.1021/cm703095z.

[25] A. Ozawa, M. Yamamoto, T. Tanabe, S. Hosokawa, T. Yoshida, Black phosphorus synthesized by solvothermal reaction from red phosphorus and its catalytic activity for water splitting, J. Mater. Chem. A 8 (2020) 7368–7376, https://doi.org/10.1039/C9TA13441G.

[26] Y. Wang, M. He, S. Ma, C. Yang, M. Yu, G. Yin, P. Zuo, Low-temperature solution synthesis of black phosphorus from red phosphorus: crystallization mechanism and lithium ion battery applications, J. Phys. Chem. Lett. 11 (2020) 2708–2716, https://doi.org/10.1021/acs.jpclett.0c00746.

[27] V.L. Deringer, C.J. Pickard, D.M. Proserpio, Hierarchically structured allotropes of phosphorus from data-driven exploration, Angew. Chem., Int. Ed. 59 (2020) 15880–15885, https://doi.org/10.1002/anie.202005031.

[28] Y. Zhu, C. Lv, Z. Yin, J. Ren, X. Yang, C.L. Dong, H. Liu, R. Cai, Y.C. Huang, W. Theis, S. Shen, D. Yang, A [001]-oriented Hittorf's phosphorus nanorods/polymeric carbon nitride heterostructure for boosting wide-spectrum-responsive

photocatalytic hydrogen evolution from pure water, Angew. Chem., Int. Ed. 59 (2020) 868–873, https://doi.org/10.1002/anie.201911503.
[29] L. Zhang, H. Huang, B. Zhang, M. Gu, D. Zhao, X. Zhao, L. Li, J. Zhou, K. Wu, Y. Cheng, J. Zhang, Structure and properties of violet phosphorus and its phosphorene exfoliation, Angew. Chem., Int. Ed. 59 (2020) 1074–1080, https://doi.org/10.1002/anie.201912761.
[30] Q. Liu, X. Zhang, J. Wang, Y. Zhang, S. Bian, Z. Cheng, N. Kang, H. Huang, S. Gu, Y. Wang, D. Liu, P.K. Chu, X.F. Yu, Crystalline red phosphorus nanoribbons: large-scale synthesis and electrochemical nitrogen fixation, Angew. Chem., Int. Ed. 59 (2020) 14383–14387, https://doi.org/10.1002/anie.202006679.
[31] R.A.L. Winchester, M. Whitby, M.S.P. Shaffer, Synthesis of pure phosphorus nanostructures, Angew. Chem., Int. Ed. 48 (2009) 3616–3621, https://doi.org/10.1002/anie.200805222.
[32] M. Ruck, D. Hoppe, B. Wahl, P. Simon, Y. Wang, G. Seifert, Fibrous red phosphorus, Angew. Chem., Int. Ed. 44 (2005) 7616–7619, https://doi.org/10.1002/anie.200503017.
[33] H. Thurn, H. Kerbs, Crystal structure of violet phosphorus, Angew. Chem., Int. Ed. 5 (1966) 1047–1048.
[34] J.Y. Yoon, Y. Lee, D.G. Kim, D.G. Oh, J.K. Kim, L. Guo, J. Kim, J. Choe, K. Lee, H. Cheong, C.U. Kim, Y.J. Choi, Y. Ma, K. Kim, Type-II red phosphorus: wavy packing of twisted pentagonal tubes, Angew. Chem., Int. Ed. 62 (2023) e202307102, https://doi.org/10.1002/anie.202307102.
[35] A.G. Ricciardulli, Y. Wang, S. Yang, P. Samorì, Two-dimensional violet phosphorus: a *p*-type semiconductor for (opto)electronics, J. Am. Chem. Soc. 144 (2022) 3660–3666, https://doi.org/10.1021/jacs.1c12931.
[36] W.L. Roth, T.W. DeWitt, A.J. Smith, Polymorphism of red phosphorus, J. Am. Chem. Soc. 69 (1947) 2881–2885.
[37] Y. Liu, Z. Hu, J.C. Yu, Liquid bismuth initiated growth of phosphorus microbelts with efficient charge polarization for photocatalysis, Appl. Catal. B- Environ. 247 (2019) 100–106, https://doi.org/10.1016/j.apcatb.2019.01.092.
[38] Z. Sun, B. Zhang, Q. Yan, Solution phase synthesis of the less-known form II crystalline red phosphorus, Inorg. Chem. Front. 9 (2022) 4385–4393, https://doi.org/10.1039/D2QI01019D.
[39] J.M. Zaug, A.K. Soper, S.M. Clark, Pressure-dependent structures of amorphous red phosphorus and the origin of the first sharp diffraction peaks, Nat. Mater. 7 (2008) 890–899, https://doi.org/10.1038/nmat2290.
[40] C. Fung, C. Er, L. Tan, A.R. Mohamed, S. Chai, Red phosphorus: an up-and-coming photocatalyst on the horizon for sustainable energy development and environmental remediation, Chem. Rev. 122 (2022) 3879–3965, https://doi.org/10.1021/acs.chemrev.1c00068.
[41] M.E. Schlesinger, The thermodynamic properties of phosphorus and solid binary phosphides, Chem. Rev. 102 (2002) 4267–4302, https://doi.org/10.1021/cr000039m.
[42] Z. Sun, H. Miao, M. Khurram, Z. Zhang, Y. Zhu, Q. Yan, Bottom-up approach to quasi-monolayer black phosphorus advancing photocatalytic H_2 evolution, Chem. Eng. J. 421 (2021) 127841, https://doi.org/10.1016/j.cej.2020.127841.
[43] Y. Zhao, H. Wang, H. Huang, Q. Xiao, Y. Xu, Z. Guo, H. Xie, J. Shao, Z. Sun, W. Han, X. Yu, P. Li, P.K. Chu, Surface coordination of black phosphorus for robust air and water stability, Angew. Chem., Int. Ed. 55 (2016) 5003–5007, https://doi.org/10.1002/anie.201512038.
[44] Y. Huang, J. Qiao, K. He, S. Bliznakov, E. Sutter, X. Chen, D. Luo, F. Meng, D. Su, J. Decker, W. Ji, R.S. Ruoff, P. Sutter, Interaction of black phosphorus with oxygen and water, Chem. Mat. 28 (2016) 8330–8339, https://doi.org/10.1021/acs.chemmater.6b03592.
[45] M.C. Watts, L. Picco, F.S. Russell-Pavier, P.L. Cullen, T.S. Miller, S.P. Bartuś, O. D. Payton, N.T. Skipper, V. Tileli, C.A. Howard, Production of phosphorene nanoribbons, Nature 568 (2019) 216–220, https://doi.org/10.1038/s41586-019-1074-x.
[46] J. Lu, B. Wang, P. Jia, W. Cheng, C. Liao, Z. Xu, L. Cheng, Y. Hu, Designing advanced 0D-2D hierarchical structure for epoxy resin to accomplish exceeding thermal management and safety, Chem. Eng. J. 427 (2022) 132046.
[47] H. Vahabi, F. Laoutid, M. Mehrpouya, M.R. Saeb, P. Dubois, Flame retardant polymer materials: an update and the future for 3D printing developments, Mater. Sci. Eng. R. Rep. 144 (2021) 100604, https://doi.org/10.1016/j.mser.2020.100604.
[48] F. Laoutid, L. Bonnaud, M. Alexandre, J.M. Lopez-Cuesta, P. Dubois, New prospects in flame retardant polymer materials: from fundamentals to nanocomposites, Mater. Sci. Eng. R Rep. 63 (2009) 100–125, https://doi.org/10.1016/j.mser.2008.09.002.
[49] Z. Duan, Y. Wang, S. Bian, D. Liu, Y. Zhang, X. Zhang, R. He, J. Wang, G. Qu, P. K. Chu, X.F. Yu, Size-dependent flame retardancy of black phosphorus nanosheets, Nanoscale 14 (2022) 2599–2604, https://doi.org/10.1039/d1nr08350c.
[50] M.M. Velencoso, A. Battig, J.C. Markwart, B. Schartel, F.R. Wurm, Molecular firefighting—how modern phosphorus chemistry can help solve the challenge of flame retardancy, Angew. Chem., Int. Ed. 130 (2018) 10608–10626, https://doi.org/10.1002/ange.201711735.
[51] W. He, P. Song, B. Yu, Z. Fang, H. Wang, Flame retardant polymeric nanocomposites through the combination of nanomaterials and conventional flame retardants, Prog. Mater. Sci. 114 (2020) 100687, https://doi.org/10.1016/j.pmatsci.2020.100687.
[52] Z. Huo, Z. Duan, X. Feng, H. Wang, H. Huang, X. Fan, R. He, X.F. Yu, J. Wang, Melamine polymerization promotes compact phosphorus/carbon composite for high-performance and safe lithium storage, Small 20 (2024) 2402483, https://doi.org/10.1002/smll.202402483.
[53] S. Huo, P. Song, B. Yu, S. Ran, V.S. Chevali, L. Liu, Z. Fang, H. Wang, Phosphorus-containing flame retardant epoxy thermosets: recent advances and future perspectives, Prog. Polym. Sci. 114 (2021) 101366, https://doi.org/10.1016/j.progpolymsci.2021.101366.
[54] X. Yue, C. Li, Y. Ni, Y. Xu, J. Wang, Flame retardant nanocomposites based on 2D layered nanomaterials: a review, J. Mater. Sci. 54 (2019) 13070–13105, https://doi.org/10.1007/s10853-019-03841-w.
[55] B. Dittrich, K. Wartig, D. Hofmann, R. Mülhaupt, B. Schartel, The influence of layered, spherical, and tubular carbon nanomaterials' concentration on the flame retardancy of polypropylene, Polym. Compos. 36 (2015) 1230–1241, https://doi.org/10.1002/pc.23027.
[56] Y. Hou, Z. Xu, R. An, H. Zheng, W. Hu, K. Zhou, Recent progress in black phosphorus nanosheets for improving the fire safety of polymer nanocomposites, Compos. Part B- Eng. 249 (2023) 110404, https://doi.org/10.1016/j.compositesb.2022.110404.
[57] Y. Jiang, J. Li, D. Li, Y. Ma, S. Zhou, Y. Wang, D. Zhang, Bio-based hyperbranched epoxy resins: synthesis and recycling, Chem. Soc. Rev. 53 (2024), https://doi.org/10.1039/d3cs00713h.
[58] S.T. Lazar, T.J. Kolibaba, J.C. Grunlan, Flame-retardant surface treatments, Nat. Rev. Mater. 5 (2020) 259–275, https://doi.org/10.1038/s41578-019-0164-6.
[59] B. Schartel, T.R. Hull, Development of fire-retarded materials—interpretation of cone calorimeter data, Fire Mater. 31 (2007) 327–354, https://doi.org/10.1002/fam.949.
[60] U. Braun, B. Schartel, Flame retardant mechanisms of red phosphorus and magnesium hydroxide in high impact polystyrene, Macromol. Chem. Phys. 205 (2004) 2185–2196, https://doi.org/10.1002/macp.200400255.
[61] B. Schartel, Phosphorus-based flame retardancy mechanisms—old hat or a starting point for future development? Materials 3 (2010) 4710–4745, https://doi.org/10.3390/ma3104710.

Supporting Information

Large-Scale Synthesis of Crystalline Phosphorus Nanosheets with Superior Air-Water Stability and Flame-Retardancy Ability

*Zunbin Duan, Rui Li, He Bian, Yanfang Wang, Xue Zhang, Ziqiang Cheng, Danni Liu, Yang Li, Shuai Zhang, Guangbo Qu, Paul K. Chu, Jiahong Wang**

1. Experimental Procedures

1.1 Redispersion of cryst-P NSs

The cryst-P NSs were re-dispersed ultrasonically. Typically, 100 mg of the cryst-P NSs were added to 100 mL of anhydrous ethanol to form a suspension and sonicated for 2 h at a constant temperature. The ultrasonic probe (1,800 W) was programmed to sonicate for 2 s every 6 s, with a 4 s of interval for safety consideration. 40% of the total power was used and the temperature was kept at 6 °C. The re-dispersed suspension was centrifuged at 500 rpm for 10 min to remove remaining aggregates.

1.2 Conductivity Test

The suspension containing 1 g of red phosphorus and 10 mL (or g) of amine was thoroughly mixed at 70 °C for 30 min to achieve dissolution equilibrium. The conductivity of the suspension contributed by ionizable species was measured by a Leici DDS-11A conductivity meter using a DJS-1VC conductance electrode with DC method at 70 °C. All the experiments were performed three times and the average conductivity was used in the data analysis.

To further evaluate the interactions between amine and red phosphorus, the amine equivalent of the amine used was calculated. The amine equivalent was the quotient of the molecular weight of the amine (*Mw*) divided by the number of active hydrogens it contained (*n*). For example, the value of the amine equivalent of *N*-ethyl-1,2-ethanediamine (*Mw*, 88.15; *n*, 3) is *Mw*/*n* = 88.15/3 = 29.38.

1.3 Stability Evaluation

The air-water stability of cryst-P NSs and BP NSs with comparable size and thickness was assessed under different conditions as described in the following.

a. Atmosphere

The single nanosheet was analyzed by atomic force microscopy (AFM). A small amount of the sample was transferred onto a Si wafer in the form of a diluted ethanol suspension. The wafer was dried and stored under ambient conditions prior to AFM which was carried out at a temperature of 25 °C and relative humidity of 37%.

b. Water-saturated air

The stability of cryst-P NSs and BP NSs in water-saturated air was conducted according to the following steps. 2~3 mg of the sample were casted on a Si wafer and dried in air. The

wafer was stored at 35 °C and saturated humidity for a certain period of time. Since the upper limit of the humidity meter was 99%, the actual humidity should be near or at saturation (*i.e.*, ≥99%). The samples were analysed by X-ray photoelectron spectroscopy (XPS) and the area under the phosphorus peaks (*e.g.*, *P 2p* and P_xO_y peaks) was determined to evaluate the stability.

c. Water and heating

The stability of cryst-P NSs (or BP NSs) in water was assessed at different temperature with the aid of the absorption spectra acquired from the nanosheet-water suspension. The temperature was 30 ºC, 40 ºC, or 50 ºC, and the nanosheet concentration was about 40 μg mL^{-1}. Absorption spectra were acquired every other day and the suspension was photographed at the same time for a total of 5 days. The stability was determined by monitoring the changes in the absorbance at 500 nm.

d. Water and bright light

The stability of the aqueous nanosheet suspension was monitored under a xenon lamp and absorption spectra were acquired at different time. The xenon lamp was placed vertically from the suspension at a distance of 30 cm. The light intensity was equivalent to about one sun (100 mW cm^{-2}). The suspension was stored in a water bath of 25 ºC to keep the temperature constant. The stability was evaluated every 2 hours for a total of 10 hours. The nanosheet concentration was calculated according to the method described in *part c*.

e. Organic solvent and long-term storage

The ethanol suspensions were analysed by XPS and lattice fringe imaging. The suspension with cryst-P NSs was stored in air for about 13 months before analysis, whereas the suspension containing BP NSs was kept in a glove box with minimum oxygen before oxidization.

1.4 Preparation of P-based Epoxy Resin and Bare Epoxy Resin

The content of cryst-P NSs (or BP NSs) in the P-based epoxy resin (EP) composite was optimized to 1.0 *wt*% based on our previously route [1]. 10.0 mL of the 15.0 mg mL^{-1} cryst-P NSs (or BP NSs) suspension in acetone was mixed with 10.0 g of epoxy resin CER1000. For the maximize dispersion of nanosheets in matrix, the obtained suspension was dispersed ultrasonically (1,000 W) for 5 min and then evenly mixed using a vortex mixer (3,000 rpm) for 10 min at RT, followed by vacuum-dried at 60 ºC for 3 h to remove acetone. The mixture was combined with 5.0 g of the curing agent CEH500 (3,000 rpm, 10 min) for further homogenization, poured into a 100 mm of length × 100 mm of width × 2 mm of height curing mold, and cured at 60 ºC for 2 h. After curing, the resulting sample was cooled to RT to obtain

the P-based EP composite designated as cryst-P NSs/EP (or BP NSs/EP). To produce the bare EP, 10.0 g of CER1000 and 5.0 g of CEH500 were mixed (3,000 rpm, 10 min), transferred to a curing mold and cured at 60 °C for 2 h.

1.5 Materials Characterization

Scanning electron microscopy (SEM) was performed on the Zeiss Supra 55 Sapphire field-emission scanning electron microscope at 5.0 kV and a working distance of 5 mm. All the SEM samples were coated with a thin layer of platinum prior to imaging to avoid charging. Transmission electron microscopy (TEM) and energy-dispersive X-ray spectroscopy (EDS) were carried out on the Tecnai G2 F20 at 300 kV. Scanning transmission electron microscopy (STEM) was performed on the FEI Themis Z Cs-corrected TEM at 120 kV. Powder X-ray diffraction (XRD) was conducted on the Rigaku SmartLab Diffractometer with Cu Kα radiation (40 kV, 30 mA, 1.54 Å). The Raman spectra were acquired on the Horiba Jobin-Yvon Lab Ram HR VIS high-resolution confocal Raman microscope equipped with a 633 nm laser as the excitation source at room temperature. The atomic force microscopy (AFM) samples were prepared by spin-coating or drop-casting an aliquot of the diluted sample-ethanol suspension on Si. An Oxford AR Cypher S atomic force microscope was operated in the tapping mode to conduct AFM. X-ray photoelectron spectroscopy (XPS) was conducted on the Thermo Fisher ESCALab 250Xi spectrometer with Al Kα radiation (1486.6 eV, 150 W). The XPS spectra were calibrated by the C 1s peak at 284.6 eV. Ultraviolet photoelectron spectroscopy (UPS) was performed on the same spectrometer with a He I radiation source (21.22 eV, 5 mm × 5 mm). The diffuse reflectance spectra were acquired on the Perkin-Elmer lambda 950 UV/Vis/NIR spectrophotometer at a scanning rate of 600 nm min^{-1} and data interval of 1.00 nm. Elemental analysis (C, H, O, and N) was conducted on the Thermo Scientific FLASH 2000 CHNS/O analyzer with He as the carrier gas. The UV-vis absorption spectra were obtained on the Hitachi U-3900 UV-vis spectrophotometer (scanning rate of 600 nm min^{-1} and data acquisition rate of 80 times s^{-1}). The water contact angles on the cryst-P NSs and BP NSs were measured on the OCA20 water contact angle instrument. Optical microscopy on the Olympus IX71 inverted microscope was employed to observe the dispersed nanosheets in the EP matrix and the samples were prepared by rapid slicing. Dynamic mechanical analysis (DMA) was conducted on the PerkinElmer Pyris Diamond DMA analyzer (tested temperature of 20–100 °C, heating rate of 5 °C min^{-1}, and frequency of 1 Hz for tensile configuration). Microscale combustion calorimeter (MCC) was acquired on the Govmark MCC-2 analyzer (heating rate of 1 °C s^{-1} and the flow rate of 80 mL min^{-1} for N_2 and 20 mL min^{-1} for O_2). The limiting oxygen

index (LOI) and the vertical burning (UL-94) were tested by the JF-5 automatic oxygen index tester and the CZ-CZF-5 horizontal vertical combustion tester, respectively. Cone calorimetry was carried out to determine the fire retarding properties of the P-based EP composites and bare EP according to ASTM E1354/ISO 5660 (heat flux of 35 kW m^{-2}; nominal duct flow rate of 0.024 m^3 s^{-1}; separation distance of 60 mm due to the low limiting oxygen index (18.0%) of bare EP and good comparison of flame-retardant parameters; sampling interval of 5 s; data analysis of triplicate average). Thermogravimetric (TG) analysis was done on the TA Q600 thermo-analyzer (heating rate of 10 °C min^{-1}, heating temperature of 50–800 ºC and flow velocity of 100 mL min^{-1}). In the combustion test in the laboratory (*ca.* 25 ºC, 37% humidity) shown in Figure 4a, the ignition source was an alcohol lamp with a flame height of approximately 25 mm for a 20-second application period and differs from the parameters of the UL-94 test (Table S5).

1.6 Simulation and Calculation

The P–N bond energy was calculated to clarify the interaction between phosphorus and different types of amino groups (primary amino, secondary amino). To simplify the calculation process, the pyramidal P_4 cluster was used to replace red phosphorus. *N*-Ethyl-1,2-ethanediamine containing one primary amino and one secondary amino and ethylenediamine containing two primary aminos were used as characteristic molecules. The structure of P_4 cluster, *N*-ethyl-1,2-ethanediamine, ethylenediamine, *N*-ethyl-1,2-ethanediamine with P_4 cluster, and ethylenediamine with P_4 cluster was optimized under the B3LYP-D3/6-311G(d, p) level[2] using Gaussian 16 A.03 software[3], and then the P–N bond energy was calculated under the level of M06-2X/def2-TZVP[4]. The P–N bond was broken evenly in the middle, and the P–N bond energy was obtained by subtracting the energy of the molecule from the sum of the energy of the two fragments.

1.7 Calculation of Flame-Retardant Parameters

For normalized performance comparison, the flame-retardant parameters including the peak of the heat release rate (*pHRR*), total heat release (*THR*), peak of smoke production rate (*pSPR*), total smoke production (*TSP*), peak of the CO production rate (*pCOPR*), and total CO production (*TCOP*) were calculated by the following equations[5]:

$$\varphi_{pHRR} = \frac{pHRR_m - pHRR}{pHRR_m \times wt\%} \times 100\% , \quad \text{(S1)}$$

$$\varphi_{THR} = \frac{THR_m - THR}{THR_m \times wt\%} \times 100\% , \quad \text{(S2)}$$

$$\varphi_{pSPR} = \frac{pSPR_m - pSPR}{pSPR_m \times wt\%} \times 100\% \,, \quad \text{(S3)}$$

$$\varphi_{TSP} = \frac{TSP_m - TSP}{TSP_m \times wt\%} \times 100\% \,, \quad \text{(S4)}$$

$$\varphi_{pCOPR} = \frac{pCOPR_m - pCOPR}{pCOPR_m \times wt\%} \times 100\% \,, \quad \text{(S5)}$$

$$\varphi_{TCOP} = \frac{TCOP_m - TCOP}{TCOP_m \times wt\%} \times 100\% \,, \quad \text{(S6)}$$

where $pHRR_m$, THR_m, $pSPR_m$, TSP_m, $pCOPR_m$, and $TCOP_m$ are the *pHRR*, *THR*, *pSPR*, *TSP*, *pCOPR*, and *TCOP* of the matrix, *pHRR*, *THR*, *pSPR*, *TSP*, *pCOPR*, and *TCOP* are the corresponding values for the composites, and *wt%* is the mass content of the nanofillers in the composites.

1.8 Calculation of CBM and VBM from XPS Results

The diffuse reflectance spectrum was converted into Tauc plots by Eq. S7:

$$(\alpha h\nu)^{1/r} = C\left(h\nu - E_g\right) \,, \quad \text{(S7)}$$

where E_g is the optical bandgap, $h\nu$ is the energy of the incident photon, C is a constant, and α is the adsorption coefficient. The exponent r denotes the nature of the transition. A value of r = 2 was used for the indirect allowed transitions as a common practice in the phosphorus allotrope analysis. For a thin film with negligible scattering and reflectance, the adsorption coefficient can be estimated by Eq. S8:

$$\alpha = 2.303\, A \,/\, t \,, \quad \text{(S8)}$$

where t is the thickness of the thin film and A is the measured absorbance.

The work function could be estimated using the difference between the full width of the ultraviolet photoelectron spectrum and the photon energy of the exciting radiation, as follows:

$$\Phi = h\nu - (E_{cutoff} - E_{edge}) \quad , \quad \text{(S9)}$$

where Φ is the absolute value of work function, $h\nu$ is the energy of the exciting radiation (i.e., He, 21.22 eV), and E_{cutoff} and E_{edge} are the secondary electron cut-off energy and energy of the Fermi edge, respectively. In a semiconductor, the lowest binding energy point is sometimes referred as the valence band edge, because the electrons of semiconductors sit at the valence band and the Fermi level is purely theoretical. This may also be the reason that in the analysis of semiconductors, Eq. S9 is claimed to show the absolute position of the valence band. Herein, we followed the traditional procedures and used the absolute position of the valence band instead of the work function. When the standard hydrogen electrode (SHE) was the reference,

$$\Phi(vs\ SHE) = \Phi(absolute) - 4.44 \,, \quad \text{(S10)}$$

Analysis of the XPS results yielded the distance between the Fermi level and valence band maximum (VBM):

$$E_{XPS,edge} = E_{Fermi} - E_{VBM}\,, \tag{S11}$$

2. Results and Discussion

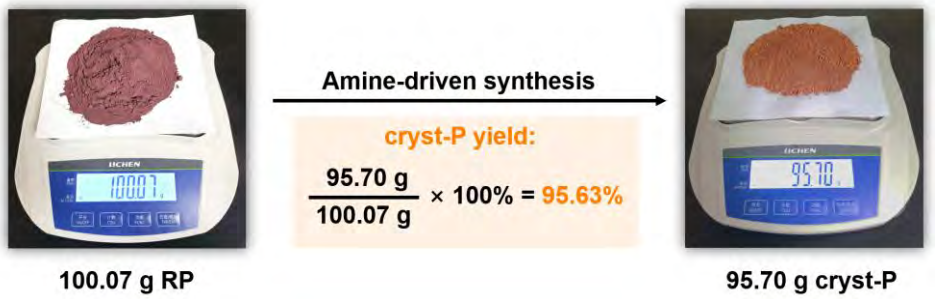

Figure S1. White light photographs and yield of 100-g-scale synthesis of cryst-P NSs. The yield of cryst-P NSs in the 100-g-scale synthesis is up to 95.6%, indicting the high conversion efficiency and great prospects for industrialization. The orange color of cryst-P may be related to the thickness in nanometer size and irregular shape. Compare to the castaneous stock RP of about 20 μm, the nano-sized cryst-P exhibit weak light absorption properties.

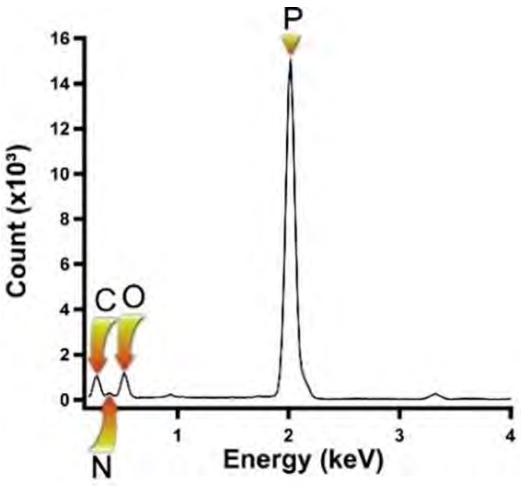

Figure S2. Elemental spectrum of cryst-P NSs revealing a large phosphorus peak and traces of C, N, and O.

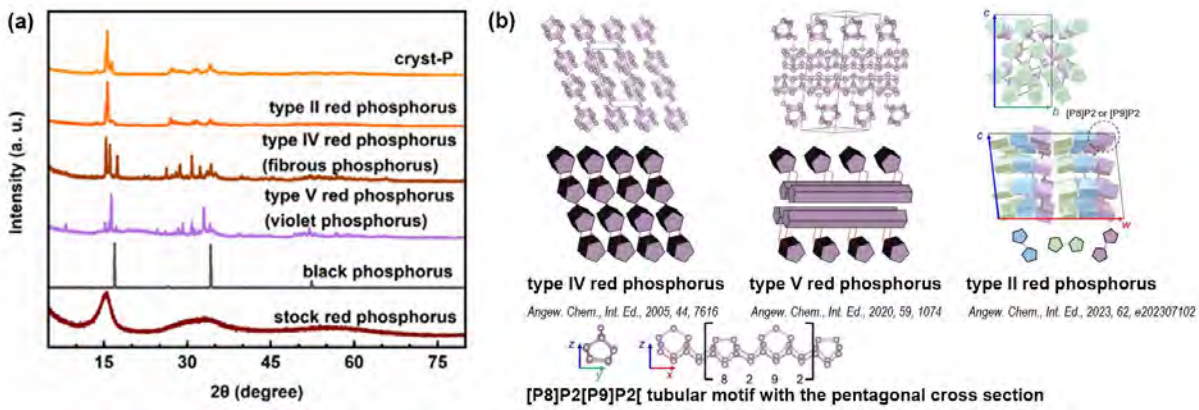

Figure S3. (a) XRD patterns of phosphorus allotropes and (b) Structural comparison of types II, IV, V red phosphorus and pentagonal [P8]P2[P9]P2[tubular motif. Red phosphorus (RP) is commonly used as a raw material for pesticides, fireworks, and organic synthesis. RP typically exists in an amorphous polymeric (type I) configuration and can be crystallized into various types of polymorphs including the known crystal structures of types II, IV, V red phosphorus. The evaluated phosphorus allotropes contain the cryst-P, stock RP, and other crystalline phosphorus synthesized by the conversional chemical vapor transmission method including types II, IV, V red phosphorus and black phosphorus. The self-synthesized cryst-P is a kind of crystalline phosphorus and highly matches the rarely reported type II red phosphorus.

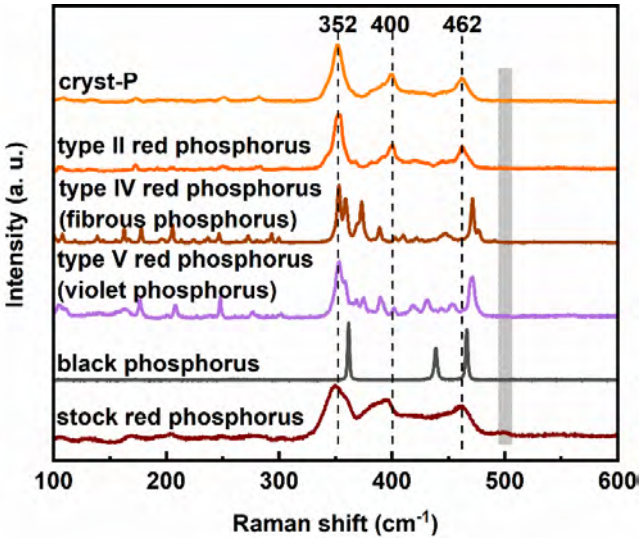

Figure S4. Raman scattering spectra of cryst-P, RP, and other crystalline phosphorus synthesized by the conversional chemical vapor transmission method. Both cryst-P (type II red phosphorus) and stock RP have characteristic Raman peaks at 352, 400, and 462 cm^{-1}, indicating that their structures contain similar constituent units. The peak at 352 cm^{-1} is attributed to the stretching vibration of P9 and P8 cages, and the peaks near 400 and 462 cm^{-1} belong to the vibration of other bonds in the structure. The Raman shift at 173 cm^{-1} is assigned to the squeezing vibration of P9 cages, while those at 278 and 247 cm^{-1} belong to the radial breathing mode. The obvious difference around 500 cm^{-1} confirms the phase transition of amorphous red phosphorus to crystalline phosphorus.

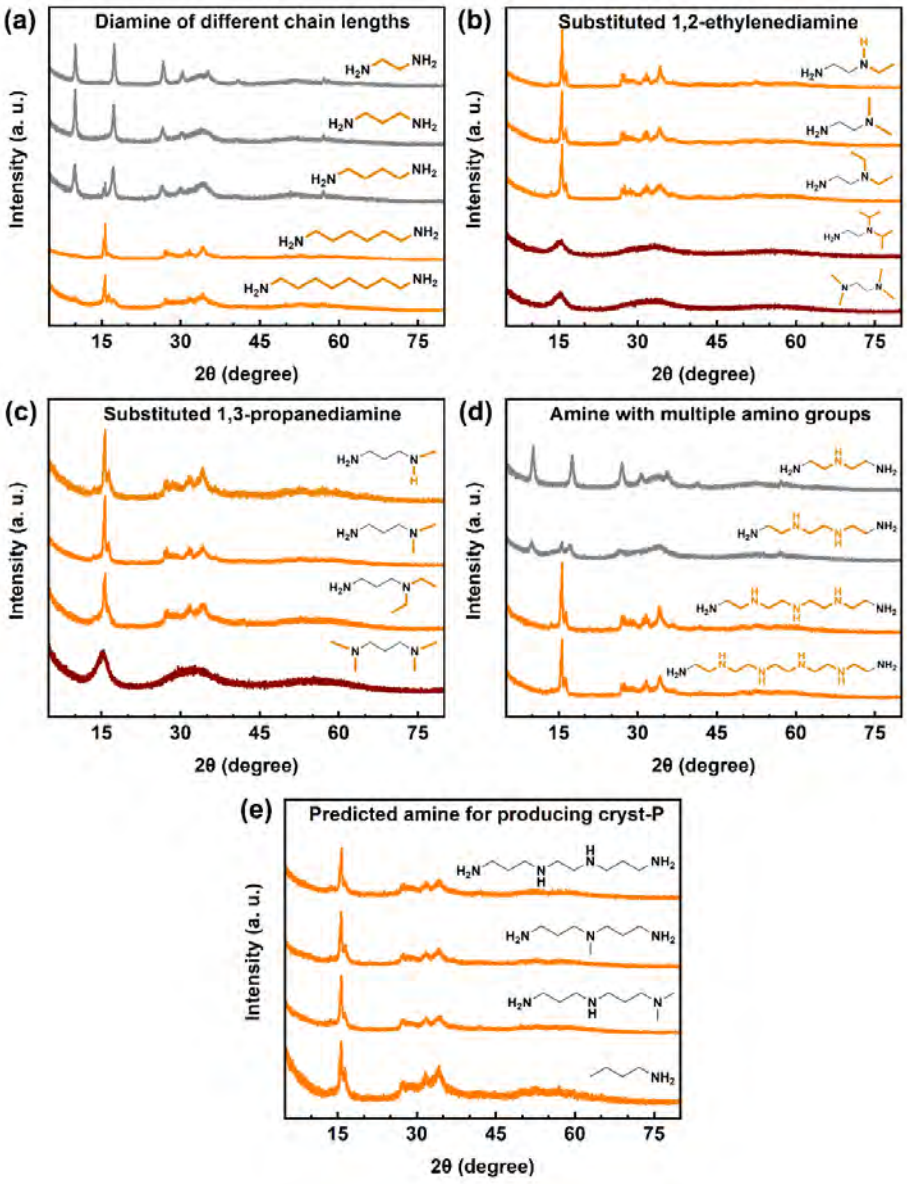

Figure S5. XRD patterns of products using different amines with RP. The amines include (a) diamine of different chain lengths, (b) substituted 1,2-ethylenediamine, (c) substituted 1,3-propanediamine, (d) amine with multiple amino groups, and (e) predicted amine for producing cryst-P. The orange line in the XRD pattern shows that the product is cryst-P. The grey line represents amine-P and the dark red line represents amorph-P.

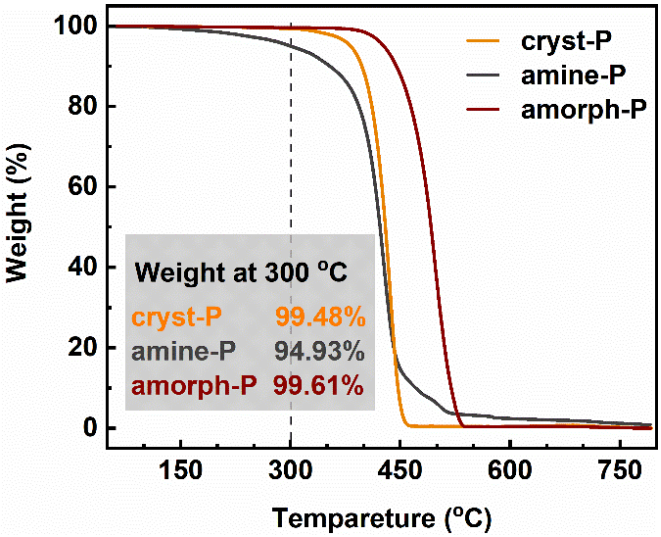

Figure S6. Thermogravimetric curves of cryst-P, amine-P and amorph-P under nitrogen. The weight of cryst-P, amine-P, and amorph-P at 300 °C is 99.48%, 94.93%, and 99.61%, respectively, indicating that the cryst-P and amorph-P have extremely high purity (**Table S1** and **Figure S2**) and the amine-P contains about 5.07% of amine.

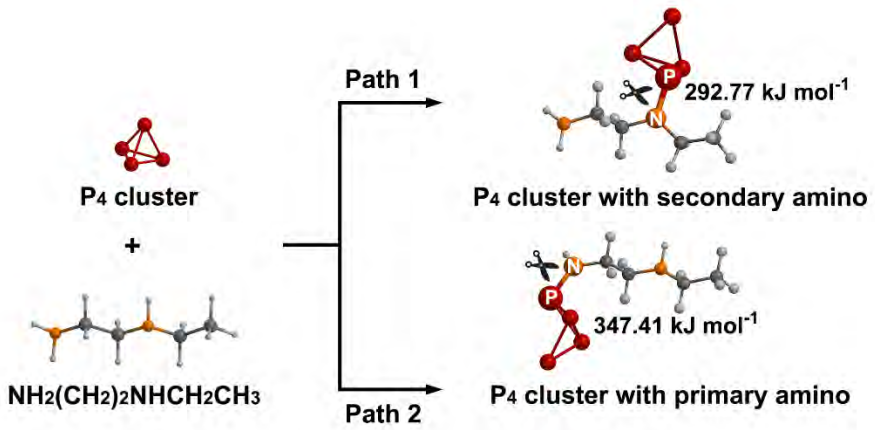

Figure S7. Activation the pyramidal P_4 cluster by secondary amino (*path 1*) or primary amino group (*path 2*).

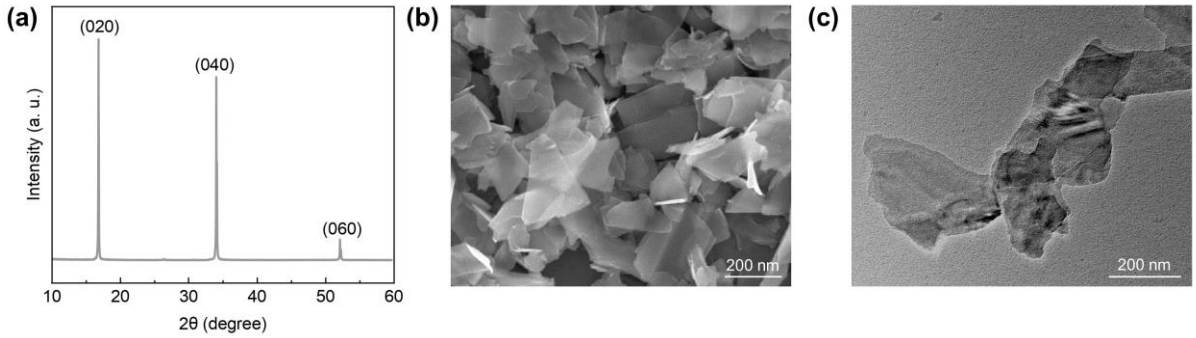

Figure S8. Structural characterization of the BP NSs used showing the crystalline nature and nanosheet morphology. (a) XRD pattern. (b) SEM image. (C) TEM image. More characterizations of the BP NSs are presented in the previous report [1].

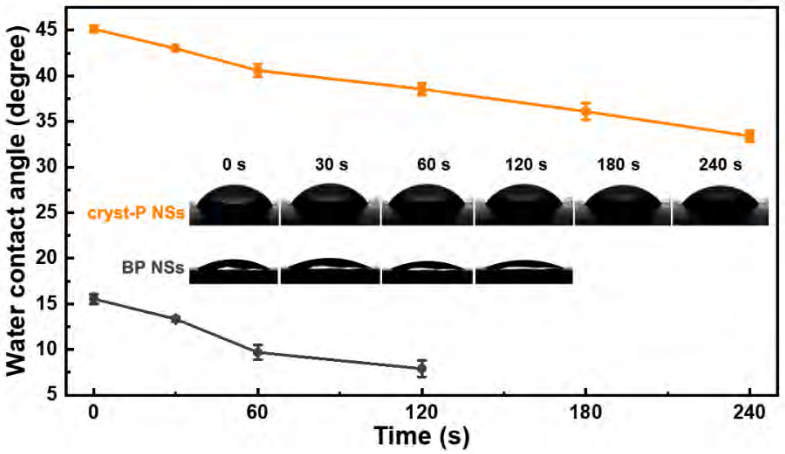

Figure S9. Water contact angles on the cryst-P NSs and BP NSs. Error bars: standard deviation of three experiments. When the contact angle is less than 7°, it is difficult to determine the angles accurately and therefore, the BP NSs are measured continuously for 120 s. The weak hydrophilicity of cryst-P NSs is advantageous for water resistance and dispersion in polymer substrates. However, elucidating the underlying mechanism for the exceptional stability of cryst-P NSs at the molecular and atomic levels is challenging due to the unconfirmed precise structure. Enhancing the hydrophobic properties of cryst-P NSs through organic surface modification, for example through melamine coating, can align with the requirements of rigorous industrial scenarios.

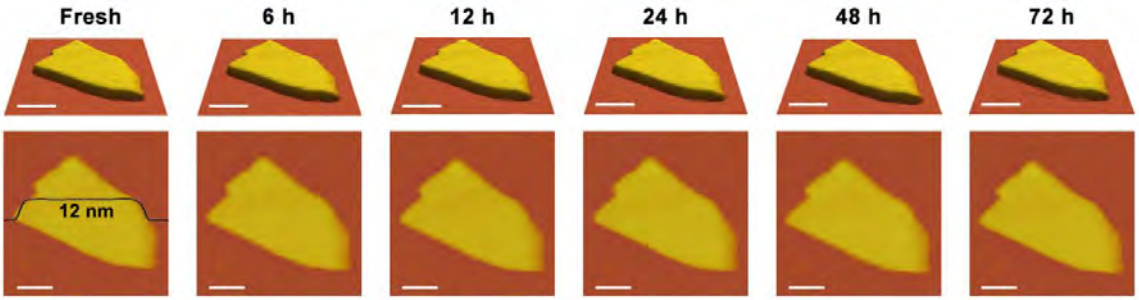

Figure S10. AFM images of the single cryst-P NS with a thickness of 12 nm aged at 25 ºC in direct contact with air (37% humidity). All scale bars are 100 nm.

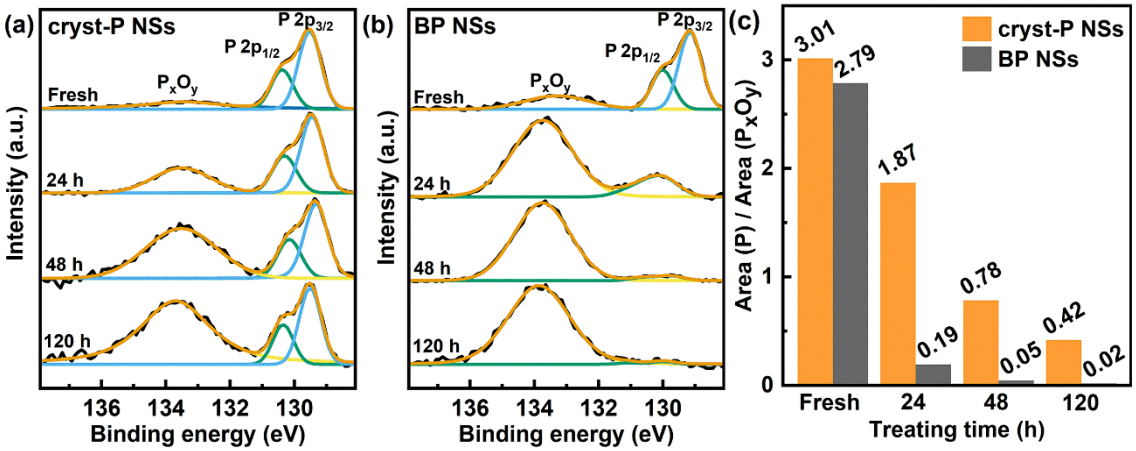

Figure S11. Stability of cryst-P NSs and BP NSs on the silicon wafer and treated at 35 °C and ≥99% humidity. (a, b) XPS spectra of (a) cryst-P NSs and (b) BP NSs. (c) Integrated area ratios of elemental phosphorus to P_xO_y.

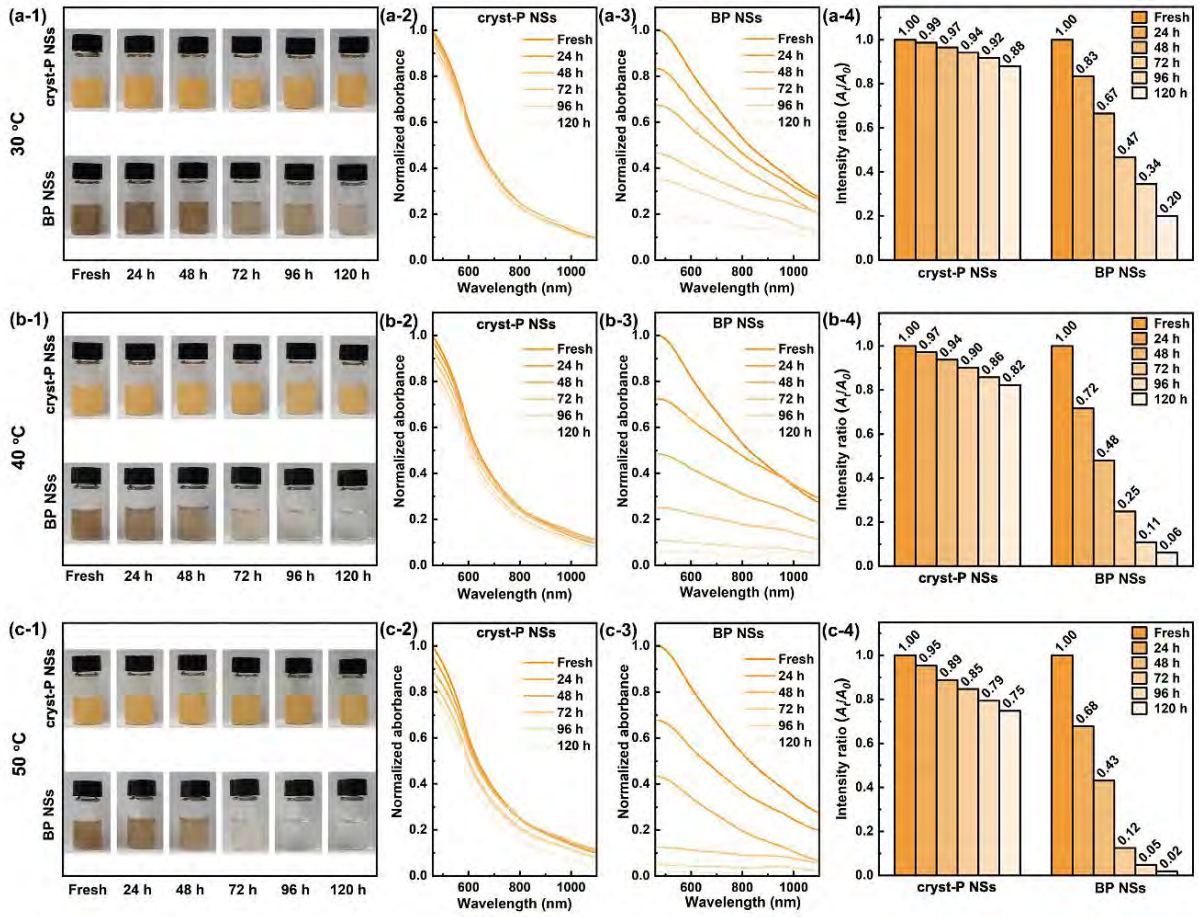

Figure S12. Stability of cryst-P NSs and BP NSs in water at different temperatures. (a) 30 ºC; (b) 40 ºC; (c) 50 ºC. (*x*-1; *x* = a, b, c) Photographs and (*x*-2, 3) absorption spectra of nanosheet-water suspensions and (*x*-4) intensity ratios converted from absorbance changes at 500 nm.

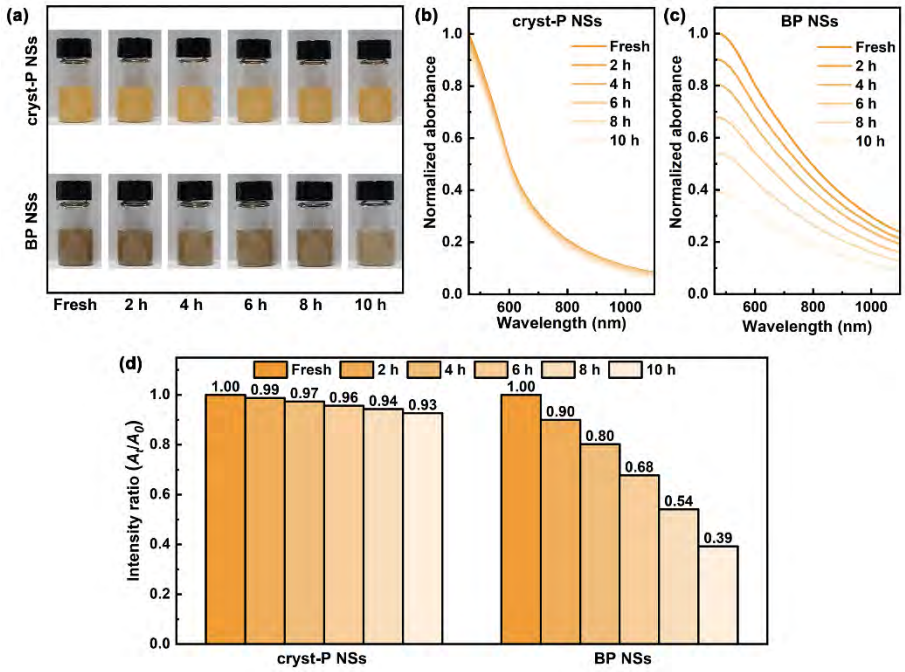

Figure S13. Stability of cryst-P NSs and BP NSs in water under xenon lamp irradiation. (a) White light photographs. (b, c) Absorption spectra of nanosheet-water suspensions. (d) Intensity ratios converted from absorbance changes at 500 nm.

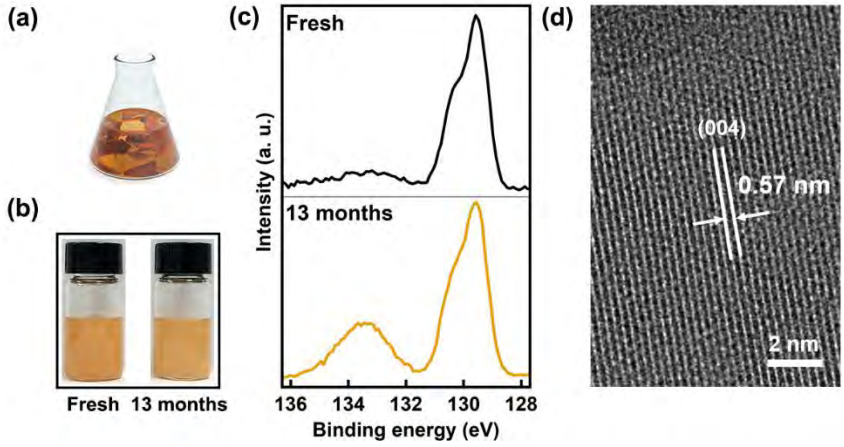

Figure S14. Stability of cryst-P NSs in ethanol. (a) Evaluation schematic diagram. (b) White light photographs of the fresh and aged cryst-P NSs suspensions. (c) XPS spectra of fresh and aged cryst-P NSs. (d) Lattice fringe image of cryst-P NSs after storage in ethanol for 13 months. Nanomaterials typically possess a large specific surface area and high surface energy, making them prone to interacting with polar solvents such as ethanol and water. As a result, they can be easily dispersed in these solvents. The ethanol suspension of the aged cryst-P NSs maintains a similar orange color and pristine crystal structure with a low oxidation degree compared to that of the fresh cryst-P NSs, indicating its good long-term storage stability in ethanol.

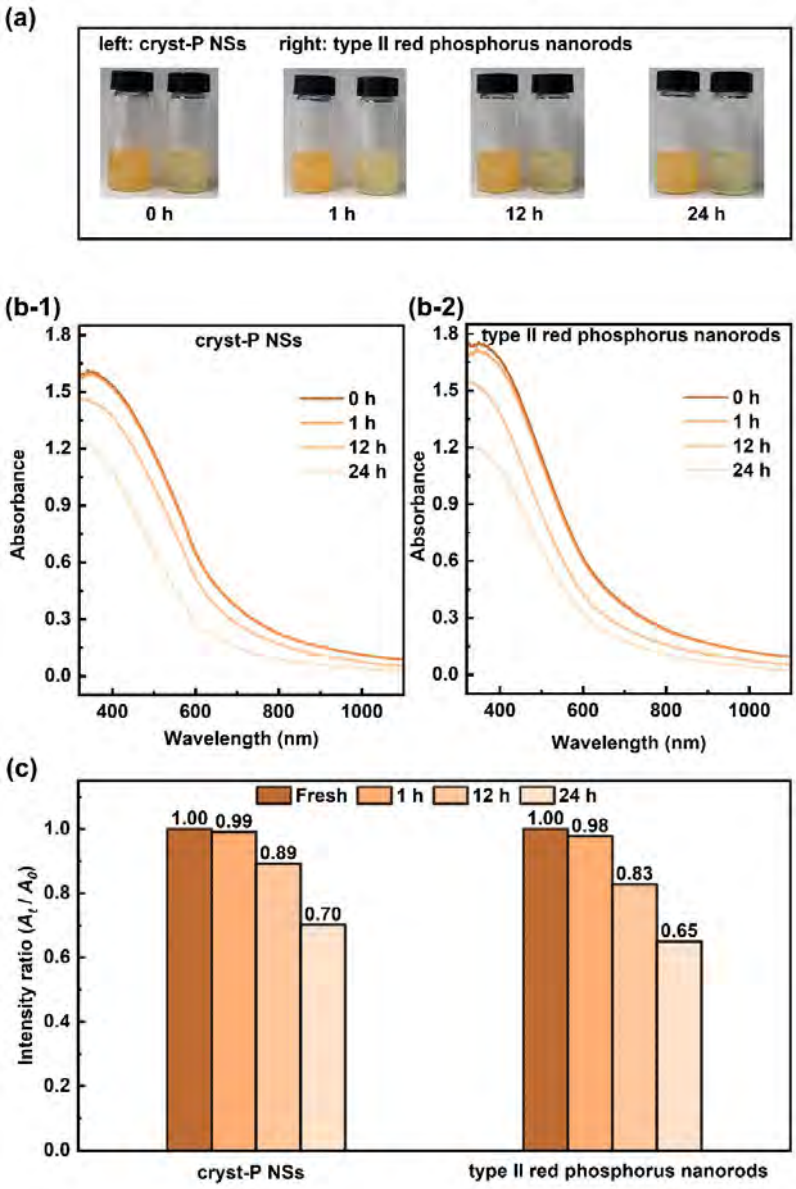

Figure S15. Stability of cryst-P NSs and type II red phosphorus nanorods in water at 60 ºC. (a) White light photographs. (b) Absorption spectra of water suspensions. (d) Intensity ratios converted from absorbance changes at 400 nm. The cryst-P NSs possess better stability in water than the type II red phosphorus nanorods, indicating that the difference in morphology affects the stability, which may be related to their probability of contacting water and oxygen molecules per unit volume.

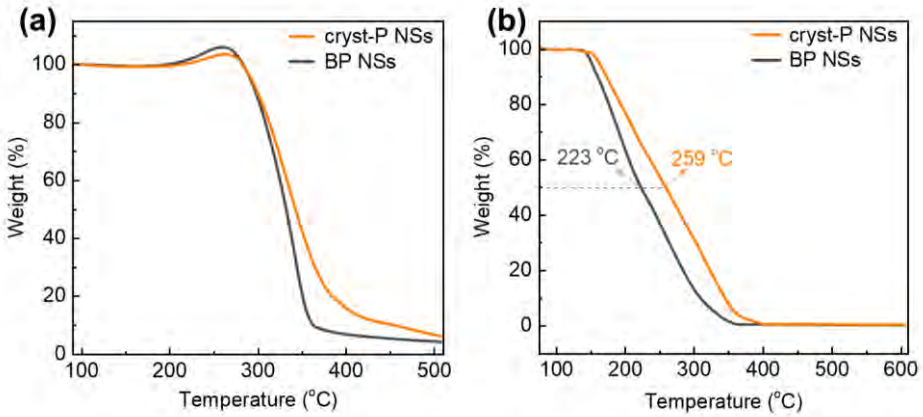

Figure S16. Thermogravimetric curves of cryst-P NSs and BP NSs under air. (a) Air after drying treatment. (b) Undried air that contains trace water. The heating rate is controlled at 20 °C min^{-1} to minimize the damage of phosphorus to the thermogravimetric equipment. The cryst-P NSs possess better thermal stability under the evaluated conditions than the BP NSs. Both the cryst-P NSs and BP NSs undergo a mass gain resulting from an exothermic process at *ca.* 200–300 °C under dried air (**Figure S16a**). This can be attributed to the partial oxidation of phosphorus nanosheets, leading to the formation of solid phosphorus oxides ($P(s) \rightarrow P_xO_y(s)$) in the absence of water [6, 7]. The cryst-P NSs exhibit a lower weight gain and a correspondingly higher temperature than the BP NSs, indicating that the cryst-P NSs are less likely to react with oxygen at elevated temperatures. However, the formation of relatively stable solid products and the observation of weight gain behavior by the cryst-P NSs and BP NSs is impeded when water is present (**Figure S16b**), may due to the high reactivity of phosphorus oxides with water resulting in the fast production of volatile substances such as phosphoric acid under elevated high temperatures [8]. The thermal stabilities of the two phosphorus nanosheets studied under dried air and undried air that contains trace water are inferior to that under nitrogen (**Figure 4b**).

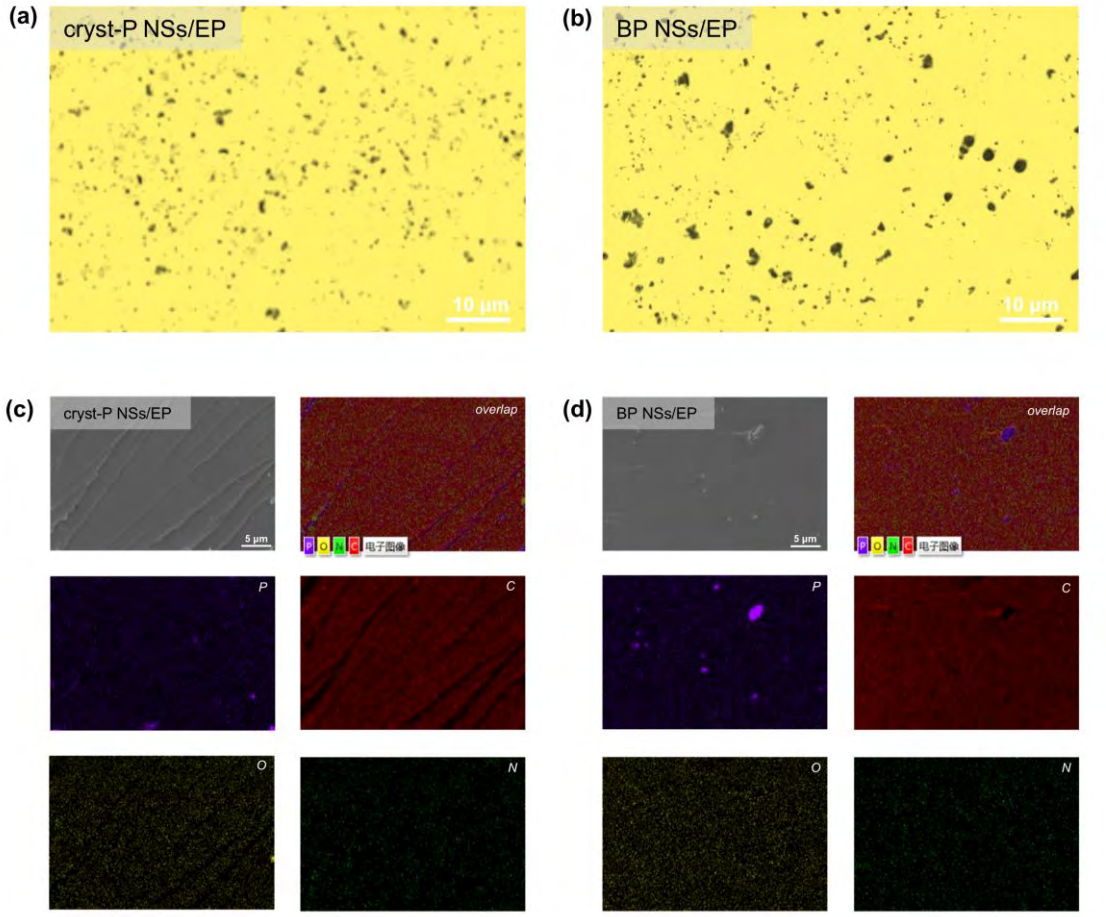

Figure S17. Dispersion of nanosheets within matrix. (a, b) Optical micrographs of (a) cryst-P NSs/EP and (b) BP NSs/EP. (c, d) SEM-mappings in cross-sections of (c) cryst-P NSs/EP and (d) BP NSs/EP. As illustrated in **Figures S17a,b**, the cryst-P NSs/EP shows a lesser degree of agglomeration of black dots in comparison to the BP NSs/EP confirming the relatively good dispersion effects of the cryst-P NSs. The same compelling evidence is discerned from the element distribution observed in the SEM-mappings of **Figures S17c,d**. The homogeneous phosphorus small aggregates are distinctly evident in the cryst-P NSs/EP, whereas the BP NSs are largely re-aggregated in the composites. Meanwhile, the rough fractured surface indicates uniform dispersion of the nanosheets in the matrix [1], and the cryst-P NSs/EP exhibits the rough fractured surface in comparison to the BP NSs/EP. Thus, the cryst-P NSs possess better dispersion within the matrix EP than the BP NSs. The dispersion of the cryst-P NSs in the matrix will be further enhanced by organic surface modification, which will be reported in a subsequent paper.

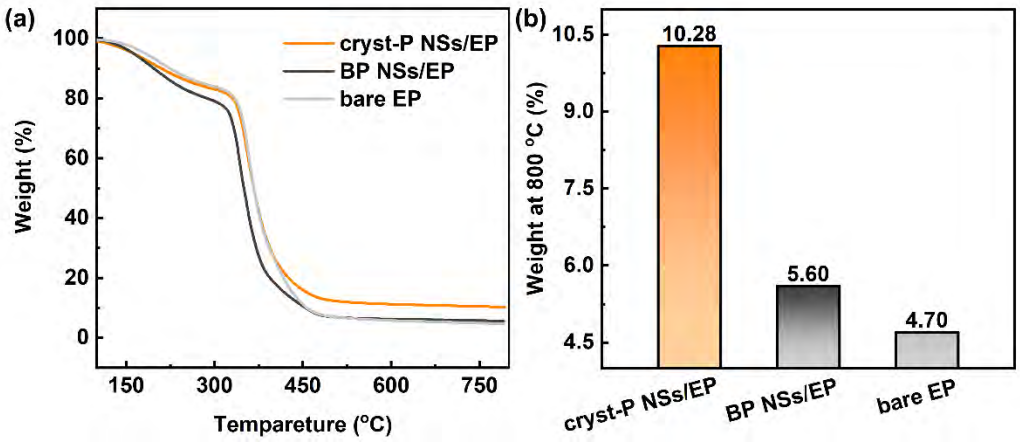

Figure S18. Thermal stability of cryst-P NSs/EP, BP NSs/EP, and bare EP under nitrogen. (a) Thermogravimetric curves and (b) Residual weights at 800 °C of P-based EP composites and bare EP.

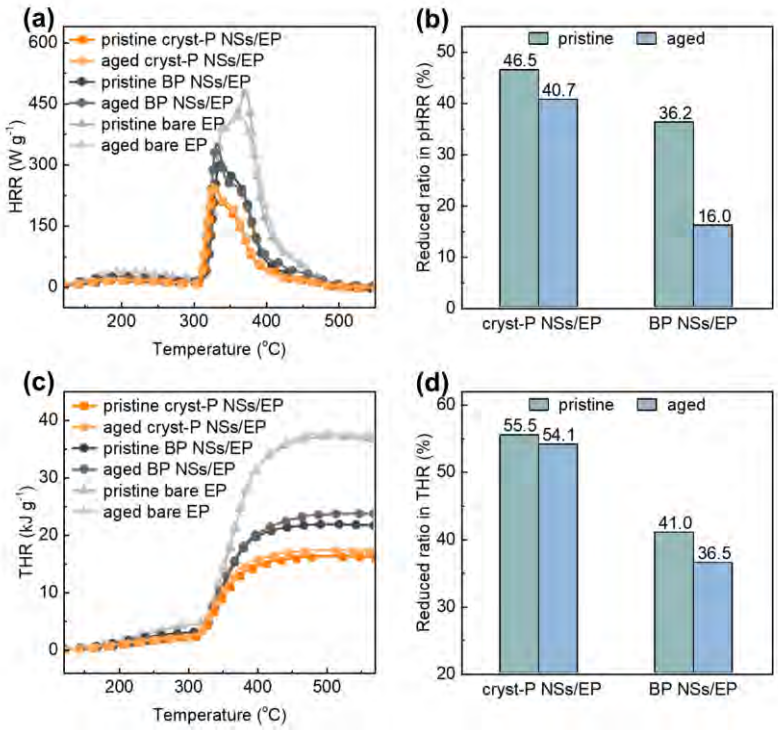

Figure S19. Combustion behaviors evaluation of EP samples before and after exposure to air by using microscale combustion calorimeter. (a) HRR curves. (b) Reduced ratio in pHRR of cryst-P NSs/EP and BP NSs/EP compared to the bare EP. (c) THR curves. (d) Reduced ratio in THR. The aged samples are obtained from the pristine samples after approximately 100 days of exposure to air at ca. 25 ºC and 37% of humidity. The aged cryst-P NSs/EP possesses closer combustion parameters of reduced ratios in pHRR and THR than the aged BP NSs/EP in comparison to the pristine EP composites, indicating the superb long-term air and water resistance of cryst-P NSs.

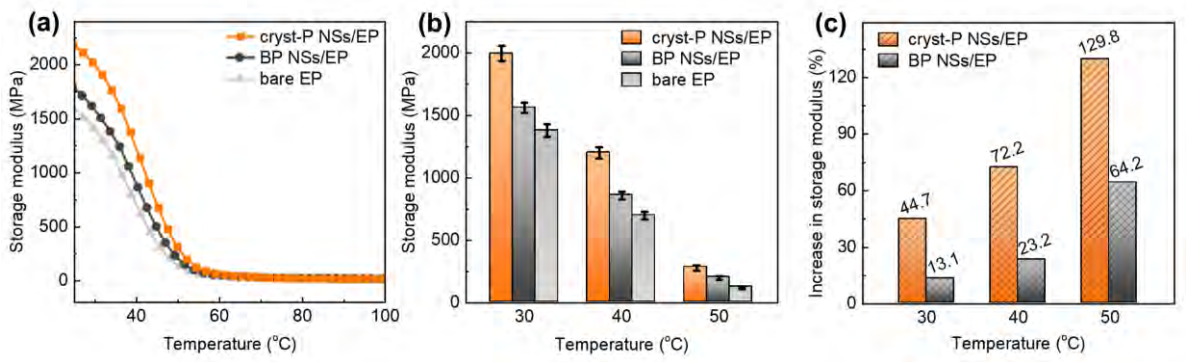

Figure S20. Mechanical properties of EP nanocomposites. (a) Storage modulus curves of cryst-P NSs/EP, BP NSs/EP, and bare EP. (b) Comparison of storage modulus at selected temperatures of 30, 40, and 50 °C. (c) Increase in storage modulus for cryst-P NSs/EP and BP NSs/EP compared to bare EP. The enhancement of storage modulus is primarily attributable to the compatibility of P-based nanosheets with epoxy resin.

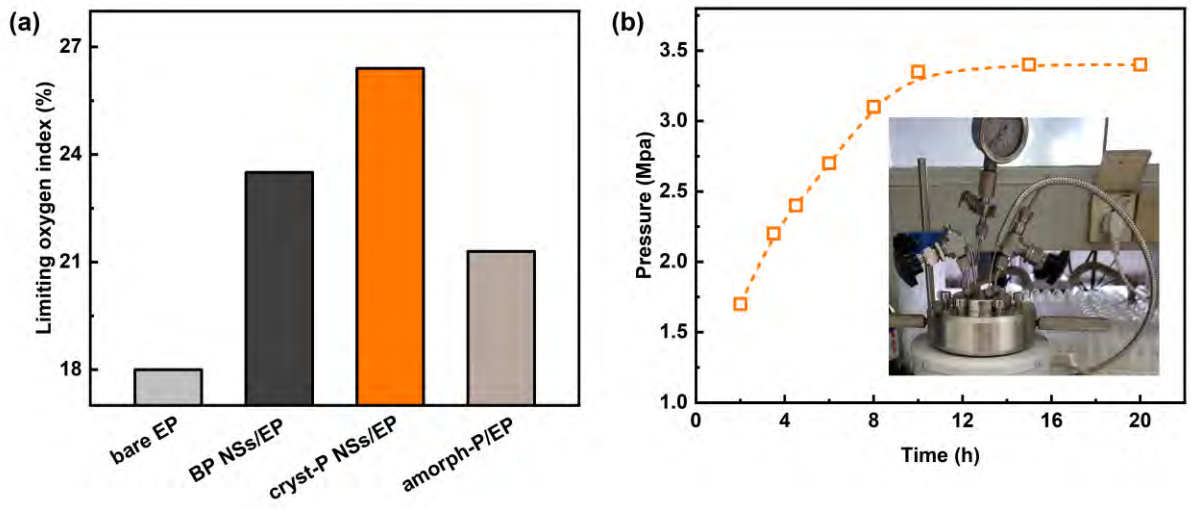

Figure S21. Limiting oxygen index and synthesis pressure evaluation. (a) Limiting oxygen index of bare EP, cryst-P NSs/EP, BP NSs/EP, and amorph-P/EP, in which amorph-P represents a commercial micron-sized amorph-P flame retardant obtained from Shenzhen Woer Heat-Shrinkable Material Co., Ltd. (b) Pressure evaluation in the synthesis of cryst-P NSs with an insert showing a white light photograph of the corresponding device (nominal volume, 100 mL; 3.0 g of raw red phosphorus and 30.0 g of tetraethylenepentamine used). Compared to the bare EP, BP NSs/EP, and amorph-P/EP, the cryst-P NSs/EP exhibits the highest limiting oxygen index (**Figure S21a**), indicating the excellent flame-retardant properties of cryst-P NSs. The maximum pressure during synthesis is approximately 3.5 Mpa (**Figure S21b**), and the amine can be recycled repeatedly, making the production of the cryst-P NSs safe and cost-effective.

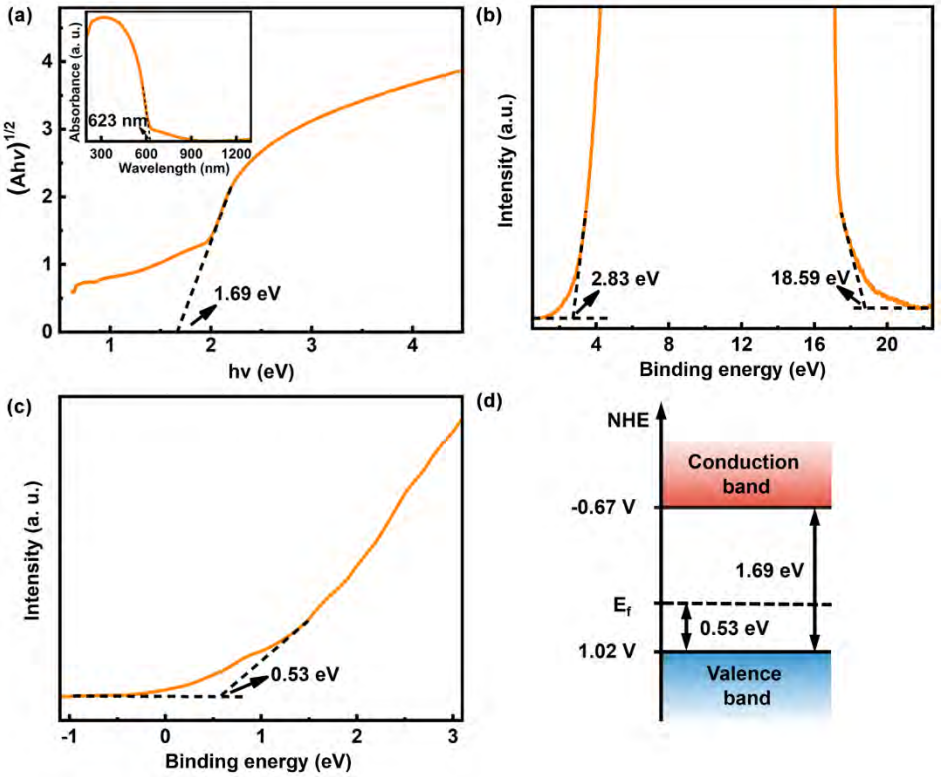

Figure S22. Band structure of cryst-P NSs. (a) Tauc plot of the cryst-P NSs with the inset showing the DRS spectrum of the cryst-P NSs. (b) UPS spectrum of the cryst-P NSs. (c) XPS VB spectrum of the cryst-P NSs. (d) Experimentally determined band diagram of the cryst-P NSs. To determine the bandgap of the cryst-P NSs experimentally, the Tauc plot is obtained by diffuse reflectance spectroscopy (DRS) (**Figure S22a**) which reveals an indirect bandgap of 1.69 eV based on the intercept, indicating that the cryst-P NSs are a nanoscale crystalline red phosphorus. Ultraviolet photoelectron spectroscopy (UPS) is employed to determine the valence band maximum (VBM) (**Figure S22b**) and X-ray photoelectron spectroscopy (XPS) is utilized to measure the gap between Fermi level and VBM (**Figure S22c**). The band structure of the cryst-P NSs is derived experimentally using the equations in the Supporting Information (Eqs. S7–S11) as illustrated in **Figure S22d**. The Fermi level of the cryst-P NSs is close to the VBM with a gap of 0.53 eV indicative of a *p*-type semiconductor. The conduction band minimum (CBM) of the cryst-P NSs (–0.67 eV) is more negative than the reaction energy of H^+/H_2 (0.00 eV), suggesting that the cryst-P NSs may be active in the photocatalytic hydrogen evolution reaction, which is discussed in detail in our other papers.

Table S1. Combustion elemental analysis of stock red phosphorus (RP, 5N purity) and as-synthesized products. The products analyzed include cryst-P powder, re-dispersed cryst-P NSs, cryst-P powder treated for 5 h at 280 ºC under argon (cryst-P 280 ºC), amine-enriched phosphorus (amine-P), and amorphous phosphorus (amorph-P). The concentrations of C, H, O, and N in all the three cryst-Ps are comparable to those of the source, suggesting a high-purity phosphorus allotrope with only a trace of adsorbed adventitious materials. The amine-P contains lots of N, O, C, and H, indicating that it is not elemental phosphorus but rather a partially oxidized phosphorus-nitrogen compound. The obtained amorph-P with trace impurities has a high probability of being a phosphorus allotrope similar to the stock RP. The five samples of RP, cryst-P powder, re-dispersed cryst-P NSs, cryst-P 280 ºC, and amorph-P are within a reasonable range of instrument background in the analytical elementals, so we infer that they are all phosphorus allotropes.

Samples	Elemental concentration (*wt*%)			
	N	C	H	O
RP	0.94	0.42	0.10	0.02
cryst-P powder	1.01	0.58	0.14	0.01
re-dispersed cryst-P NSs	0.89	0.47	0.15	0.03
cryst-P 280 ºC	0.95	0.60	0.11	0.02
amine-P	3.12	1.64	0.47	0.58
amorph-P	1.02	0.51	0.12	0.04
instrument background	0.85 ± 0.19	0.47 ± 0.16	0.10 ± 0.02	0.03 ± 0.01

Table S2. Conductivity of the red phosphorus suspension in amine, and the amine equivalent values of the amine used. The appropriate conductivity may indicate the formation of product fragment primitives. The conductivity value of the amine suspension containing red phosphorus for producing cryst-P is 0.087 – 26.6 μS cm^{-1} at 70 °C with a phosphorus-amine ratio of 0.1 g mL^{-1} and the amine equivalent value for producing cryst-P is 27.04 – 65.12.

Amine	Product	Conductivity (μS cm^{-1})	Amine equivalent
Diamine of different chain lengths			
	amine-P	3650 ± 124	15.02
	amine-P	966 ± 18	18.53
	amine-P	84.4 ± 1.4	22.04
	cryst-P	3.41 ± 0.21	29.05
	cryst-P	0.221 ± 0.004	36.06
Substituted 1,2-ethylenediamine			
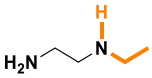	cryst-P	26.6 ± 0.5	29.38
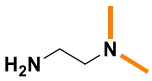	cryst-P	3.66 ± 0.14	44.08
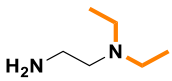	cryst-P	0.529 ± 0.051	58.10
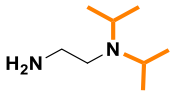	amorph-P	0.055 ± 0.004	72.13
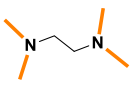	amorph-P	0	–
Substituted 1,3-propanediamine			
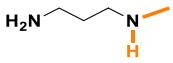	cryst-P	25.2 ± 0.5	29.38
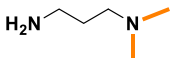	cryst-P	0.372 ± 0.024	51.09
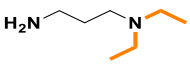	cryst-P	0.087 ± 0.008	65.12

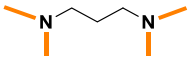	amorph-P	0	–
Amine with multiple amino groups			
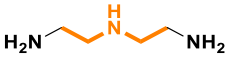	amine-P	752 ± 24	20.63
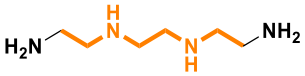	amine-P	117.2 ± 1.5	24.37
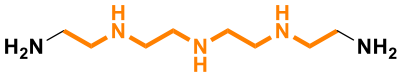	cryst-P	10.9 ± 0.1	27.04
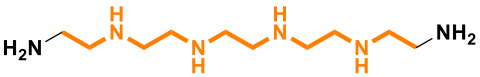	cryst-P	8.24 ± 0.32	29.05
Predicted amine for producing cryst-P			
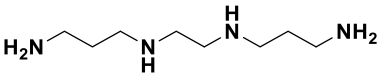	cryst-P	20.6 ± 1.0	29.05
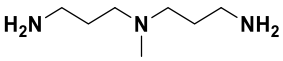	cryst-P	3.65 ± 0.08	36.31
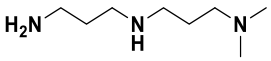	cryst-P	0.966 ± 0.014	53.09
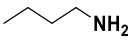	cryst-P	1.79 ± 0.12	36.57

398

399

Table S3. P–N bond energy and bond length of amine with P_4 cluster. The P–N bond energy (292.77 kJ mol^{-1}) of the secondary amino with the P_4 cluster is less than that (347.41 or 348.61 kJ mol^{-1}) of the primary amino, indicating that the bond formed by the secondary amino is easier to break to produce cryst-P, which is further confirmed by the bond length.

Species	P–N bond energy (kJ mol^{-1})	P–N bond length (Å)
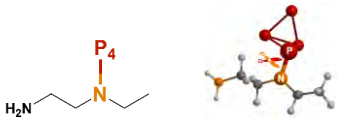	292.77	1.726
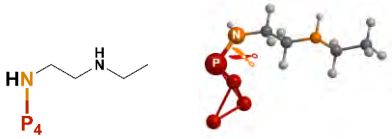	347.41	1.704
	348.61	1.701

407

408 **Table S4.** XPS results of cryst-P NSs and BP NSs treated at 35 °C and ≥ 99% humidity.

Samples	Treatment time (h)	*Area (P)*	*Area (P_xO_y)*	*Area (P)* / *Area (P_xO_y)*
cryst-P NSs	Fresh	128.50	42.63	3.01
	24	131.52	70.38	1.87
	48	135.29	172.71	0.78
	120	120.71	289.12	0.42
BP NSs	Fresh	127.68	45.82	2.79
	24	44.30	229.78	0.19
	48	9.99	216.13	0.05
	120	4.77	254.54	0.02

409

410

Table S5. Limit oxygen index and UL-94 rating evaluation of bare EP and its nanocomposites.

Samples	LOI (%)	UL-94 rating
cryst-P NSs/EP	26.4 ± 0.4	V-1
BP NSs/EP	23.5 ± 0.2	V-2
bare EP	18.0 ± 0.3	no rating

Notes: LOI, limit oxygen index, error bars of standard deviation of five tests. UL-94 test is the subject of an international standard (IEC 60695-11-10) for small flames [9]. The burner is controlled to produce a blue flame with a 20 mm high central cone and a power of 50 W. The flame is applied to the bottom of the specimen and the top of the burner has to be located at 10 mm from the bottom edge of the specimen. The flame is applied for 10 s and removed, and the afterflame time t_1 (the time required for the flame to extinguish) is noted. After extinction, the flame is applied for another 10 s. The afterflame time t_2 is noted, together with the afterglow time t_3 (the time required for the fire glow to disappear). UL-94 V-1, t_1 and t_2 less than 30 s for each specimen, $t_1 + t_2$ less than 250 s for the five specimens, $t_2 + t_3$ less than 60 s for each specimen, no afterflame or afterglow up to the holding clamp, no burning drops; UL-94 V-2, t_1 and t_2 less than 30 s for each specimen, $t_1 + t_2$ less than 250 s for the five specimens, $t_2 + t_3$ less than 60 s for each specimen, no afterflame or afterglow up to the holding clamp, burning drops allowed.

425

426 **Table S6.** Comparison of the flame retarding properties of cryst-P NSs and reported 2D flame
427 retarding nano-additives.

Nanofiller	Fraction (*wt%*)	φ_{pPHR}	φ_{THR}	φ_{pSPR}	φ_{TSR}	φ_{pCOPR}	φ_{TCOP}	Matrix	Ref.
cryst-P NSs	1.0	24.3%	21.6%	59.7%	35.6%	47.1%	35.6%	EP	This work
BP-RuL_3	3.0	20.7%	11.7%	13.2%	13.1%			EP	[5]
BNTP	0.3	19.4%	17.5%					EP	[10]
Ar@BP	1.5		30.4%		24.4%		33.2%	EP	[11]
BP-ZrPZN	2.0	56.8%	54.1%	42.9%	62.7%	34.6%		EP	[12]
BP-PA	2.0	64.6%	47.6%					CNF	[13]
BP-PZN	2.0	29.7%	31.8%					EP	[14]
BP-RGO	2.0	27.6%	27.2%		14.2%			EP	[15]
BP-OH@HAP	2.0	47.0%	23.1%					UPR	[16]
BP-PEI	2.0	17.2%	10.6%	18.2%	11.2%		25.1%	WPU	[17]
BP-CN_x	2.0	23.9%	24.8%		4.2%			EP	[18]
BP-HAN	2.0	28.0%	24.1%		25.4%		25.0%	EP	[19]
GO-DOPO	2.0	13.5%	16.2%		15.5%			EP	[20]
MoS_2-CNT	2.0	13.5%	15.5%					EP	[21]
$Ti_3C_2T_x$	2.0	27.5%	29.4%				22.2%	EP	[22]

428

3. References

[1] Z. Duan, Y. Wang, S. Bian, D. Liu, Y. Zhang, X. Zhang, R. He, J. Wang, G. Qu, P K. Chu, X. Yu, *Nanoscale* **2022**, *14*, 2599-2604.

[2] M. J. Frisch, G. W. Trucks, H. B. Schlegel, G. E. Scuseria, M. A. Robb, J. R. Cheeseman, G. Scalmani, V. Barone, G. A. Petersson, H. Nakatsuji, *Wallingford CT* **2016**, *2*.

[3] S. Grimme, J. Antony, S. Ehrlich, H. Krieg, *J. Chem. Phys.* **2010**, *132*, 154104.

[4] Y. Zhao, D. G. Truhlar, *Theor. Chem. Acc.* **2008**, *120*, 215-241.

[5] Z. Qu, K. Wu, W. Meng, B. Nan, Z. Hu, C. Xu, Z. Tan, Q. Zhang, H. Meng, J. Shi, *Chem. Eng. J.* **2020**, *397*, 125416.

[6] Z. Zhang, X. Xin, Q. Yan, Q. Li, Y. Yang, T. Ren, *Sci. China Mater.* **2016**, *59*, 122-134.

[7] X. Zhang, Z. Zhang, S. Zhang, D. Li, W. Ma, C. Ma, F. Wu, Q. Zhao, Q. Yan, B. Xing, *Small* **2017**, *13*, 1701210.

[8] R. N. Bell, *Ind. Eng. Chem.* **1948**, *40*, 1464-1467.

[9] F. Laoutid, L. Bonnaud, M. Alexandre, J. M. Lopez-Cuesta, P. Dubois, *Mater. Sci. Eng. R.* **2009**, *63*, 100-125.

[10] J. Pan, M. Wu, Y. Zheng, H. Chu, X. Liu, S. Liu, J. Zhao, W. Xie, *Chem. Eng. J.* **2023**, *476*, 146463.

[11] K. Wang, X. Li, G. Yuan, Z. Liu, H. Yang, Z. Li, W. Diao, F. Xiao, K. Wu, J. Shi, *Small* **2023**, *19*, 2301430.

[12] S. Qiu, W. Yang, X. Wang, Y. Hu, *Chem. Eng. J.* **2023**, *453*, 139759.

[13] R. Wang, J. Ma, S. Ma, Q. Zhang, N. Li, M. Ji, T. Jiao, X. Cao, *Chem. Eng. J.* **2022**, *450*, 137985.

[14] S. Qiu, Y. Zhou, X. Zhou, T. Zhang, C. Wang, R. K. K. Yuen, W. Hu, Y. Hu, *Small* **2019**, *15*, 1805175.

[15] Y. Zhou, F. Chu, S. Qiu, W. Guo, S. Zhang, Z. Xu, W. Hu, Y. Hu, *J. Hazard. Mater.* **2020**, *399*, 123015.

[16] Y. Zhou, L. Wang, L. Ding, W. Yang, C. Zhang, D. Liu, W. Hu, Y. Hu, *ACS Materials Lett.* **2023**, *5*, 2870-2876.

[17] L. He, X. Zhou, W. Cai, Y. Xiao, F. Chu, X. Mu, X. Fu, Y. Hu, L. Song, *Compos. Part B: Eng.* **2020**, *202*, 108446.

[18] X. Ren, B. Zou, Y. Zhou, Z. Zhao, S. Qiu, L. Song, *J. Colloid Interface Sci.* **2021**, *586*, 692-707.

[19] S. Qiu, Y. Hou, X. Zhou, Y. Zhou, J. Wang, B. Zou, W. Yang, L. Song, Y. Hu, *Chem. Eng. J.* **2021**, *425*, 131532.

[20] Y. Feng, X. Li, X. Zhao, Y. Ye, X. Zhou, H. Liu, C. Liu, X. Xie, *ACS Appl. Mater. Interface* **2018**, *10*, 21628-21641.

[21] K. Zhou, J. Liu, Y. Shi, S. Jiang, D. Wang, Y. Hu, Z. Gui, *ACS Appl. Mater. Interface* **2015**, *7*, 6070-6081.

[22] J. Lu, B. Wang, P. Jia, W. Cheng, C. Liao, Z. Xu, L. Cheng, Y. Hu, *Chem. Eng. J.* **2022**, *427*, 132046.